UNIVERSITÀ DEGLI STUDI DI PADOVA

SCUOLA DI SCIENZE

DIPARTIMENTO DI GEOSCIENZE

Corso di Laurea Magistrale in Geologia Ambientale e Dinamica della Terra (LM-74)

Curriculum Earth Dynamics

Microstructural analysis of microboudinaged biotite porphyroblasts in graphitic schists from the SW Tauern Window (Valle di Vizze)

Relatore: Prof. Bernardo Cesare

Correlatore: Prof. Omar Bartoli

Correlatore: Prof. Whitney Behr

Correlatore: Dr. Leif Tokle

Laureando: Leonardo Salvadori

Anno Accademico: 2022/2023

Abstract

This study is aimed at the microstructural analysis and at the reconstruction of the deformation history of some peculiar microboudinaged biotite porphyroblasts from the south-western Tauern Window (Passo di Vizze, Italy). In the past, similar structures from other localities have been highlighted and studied, but not in much detail. My analysis aims at a better understanding of the formation of these microstructures with not only a qualitative overview of the microstructural setting shown by the rock only, but also with quantitative data such as strain reconstruction, aspect ratio analysis and shape and orientation analysis.

The studied schists (Furtschaglschiefer *Auct.*) derive from a pelitic protolith in the SW Tauern Window that was metamorphosed under upper greenschists to lower amphibolite facies conditions during the Alpine orogenesis. Biotite appears in many different microstructural settings, but it is possible to define three main types: the "foliation-perpendicular" microboudinaged biotites (type I), the fanned *mica-fish* biotites (type II) and the foliation-parallel elongated biotites (type III). The microboudinaged biotites are the coarser in size (up to 1 cm), and typically show alternating graphite-rich sectors separated by clean biotite and sometimes quartz. The sectors, as well as biotite cleavage planes, are perpendicular to the foliation while the graphite inclusions are parallel to it. Fanned biotites and elongated biotites are showing inclined and foliation-parallel cleavages, respectively. Other porphyroblasts such as garnet and ilmenite have also been studied and provide information on the relative timing and the metamorphism/deformation relations.

The fabric analysis was performed using 2D data collected during detailed petrographic analysis on several oriented thin sections and using 3D data collected with Micro X-ray Computed Tomography on a 2x3x1 rock volume. The collected data allowed to reconstruct the strain that the rock was subjected to, the relations between quartz/biotite ratio and the total strain, the relations between aspect ratio and the orientation of crystals, and the shape analysis of biotite and ilmenite porphyroblasts.

The qualitative petrographic observations and the 2D and 3D data have been integrated in order to understand the deformation mechanism(s) that led to the formation of the microstructure. The analysis revealed that microboudinage coupled with rotation of the porphyroblast are the principal deformation mechanisms for type I and II. The rotation timing for type II biotites is still uncertain. For type III biotites, it is not possible to distinguish whether they are elongated due to recrystallization or due to deformation

Acknowledgments

Index

1 Introduction

Regional metamorphism is a dynamo-thermal process and as such, deformation and recrystallization are its principal mechanisms. They play different roles to different extents and may result in different structures but nonetheless act together (Rutter & Brodie, 1995; Hobbs et al., 2010; Lardeaux, 2023). The study of deformed metamorphic rocks is useful in the definition of the regional tectonic and the pressure (P) – temperature (T) conditions at which the rock experienced recrystallization and/or deformation. Deformed rocks constitute one of the few direct evidences obtainable for tectonic reconstructions, and the study of the overprinting relations can be linked to the deformation phases and the metamorphic events (Passchier & Trouw, 2005). At a larger scale, we can correlate these to tectonic and metamorphic events during orogenic processes (Passchier & Trouw, 2005). Deformational structures are not always visible at the outcrop scale or at the hand sample scale and very often we need to look at microstructures in order to understand the deformation phases and how they operated in a rock body in relation to its metamorphism.

Moreover, a microstructural analysis can provide information on the deformation mechanism(s) that acted on the rock and help retrieve the deformational history.

The study of deformation/metamorphism relations is usually carried out on porphyroblasts. These minerals are grown in a fine-grained matrix and are larger crystals formed during metamorphism.

Zwart (1960) proposed a first classification for the definition of the relative timing of porphyroblasts growth in relation to a specific deformation phase. In this work, I will refer to pre-, inter-, syn- and post-tectonic (or kinematic) porphyroblasts in the sense of Passchier and Trouw (2005, Fig. 1.1 modified after Zwart 1960).
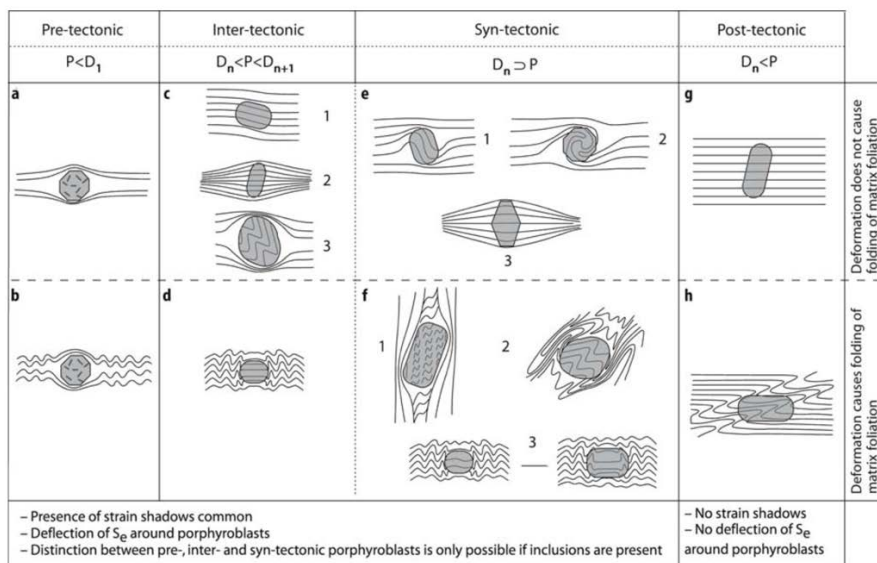

Fig. 1.1: schematic description of pre-, intra-, syn- and post-tectonic porphyroblast growth

The presence of strain shadows and deflection of the external foliation are characteristics of pre-, inter and syn-tectonic porphyroblast but they can be distinguished only if inclusions are present. Pre-tectonic porphyroblast are usually showing a casual distribution of inclusions, inter-tectonic porphyroblast are characterized by high-angle internal foliation in respect to the main foliation and syn-tectonic porphyroblast show inclusions trails that are curved and/or continuous with the external foliation. Post-tectonic porphyroblast are usually showing continuous inclusion trails and no strain shadow or deflection of the external foliation.

Among all porphyroblasts, garnet is by far the most widespread and useful mineral that provides many insights for the tectonic reconstruction due to its ability of including other minerals and to develop evident inclusion trails (e.g., snowball garnets).

In this work, biotite porphyroblasts are the main subjects. Although not as common as garnet, biotite can also have porphyroblastic characteristics that are useful for a reconstruction of the tectonic events, the metamorphism/deformation relation and the deformation mechanism. In this case, within pelitic schists from the SW Tauern Window (eastern Alps, Italy), biotite porphyroblast are showing inclusion that are continuous with the external foliation and an evident microboudinaged structure. The latter is also an excellent strain marker that allows to reconstruct the amount of deformation the rock was subjected to.

Not much work has been done on similar microstructures (Lister et al., 1985; Miyake, 1992; Little et al., 2002;, Kim & Cho, 2008; Camilleri, 2009), and so this work aims at a further expansion of the subject through 2D and 3D microstructural analysis by means of thin section petrography, SEM observations and computed microtomography.

2 Geological setting

2.1 The Eastern Alps and the Tauern Window

The Alps are one of the most studied collisional belts. The development of the belt began during the Cretaceous when the Adriatic and European continental margins started to converge. The convergence of the two plates resulted in the complete closure of the Neotethys and testifies the beginning of the continent-continent collision (Dal Piaz et al. 2003).

The structure of the Alps is defined by several tectonic nappes. Following Dal Piaz et al. (2003) the Europe-vergent tectonic domain of the Alps can be divided, from top to bottom and from the inner side to the outer side, in: the Austroalpine zone, the Penninic zone and the Helvetic zone. The Southern Alps (or Southalpine domain) are antithetic and are found to the south of the Periadriatic Lineament.

The Austroalpine zone derives from the distal portion of the Adriatic continental margin while the Penninic zone is composed by nappes coming from both the Tethyan oceanic lithosphere and the European passive margin. The Helvetic zone derives instead from the proximal portion of the European margin and consists of shallow basement and detached cover units. Finally, the Southern Alps are the deformed passive margin of the belt and are unaffected by Alpine metamorphism (Dal Piaz et al., 2003; Schmid et al., 2004). Figure 2.1 shows the principal tectonic domains of the Alps.
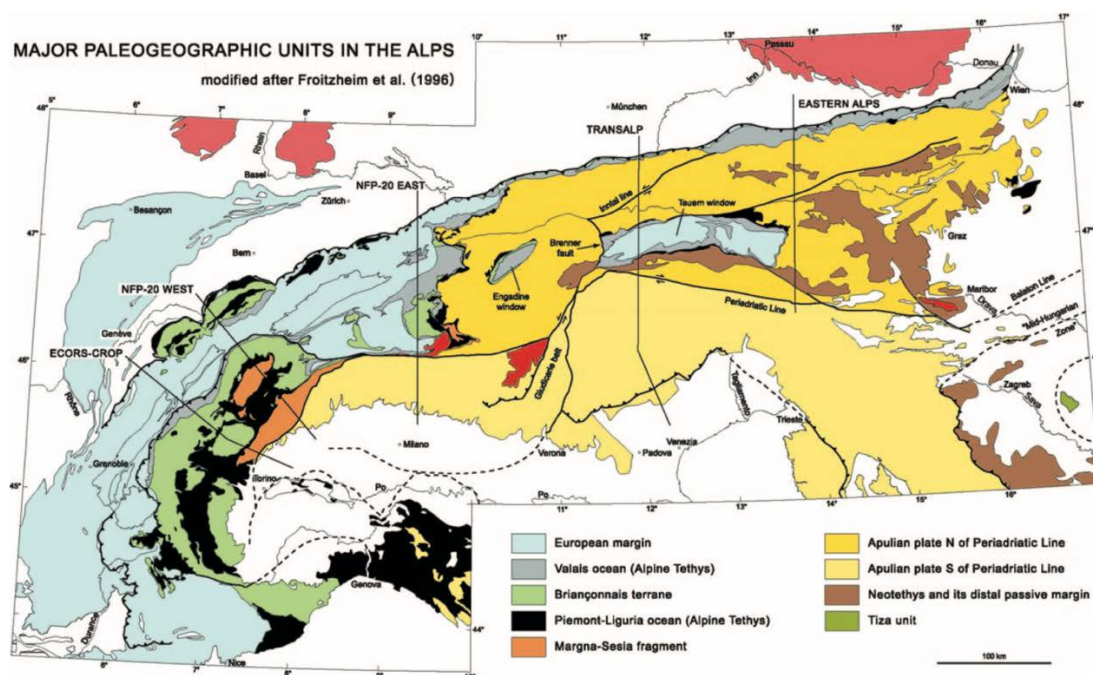

Fig. 2.1: Major paleogeographic and tectonic units of the Alps (Schmid et al., 2004).

The Tauern Window (TW) is located in the Eastern Alps. It is a tectonic window where the structurally lower Pennic units are exposed, surrounded by the overlying Austroalpine basement. This structure was formed by a significant and contemporaneous Cenozoic orogen-parallel extension and orogen-perpendicular compression (Selverstone, 1988; Ratschbacher et al., 1989). The extensional component of deformation was accommodated by an east-directed set of strike-slip faults, resulting in a lateral extrusion toward the east. The Tauern Window is bounded by low-angle normal faults on the east (Katschberg fault - Ka in Figure 2.2) and west (Brenner fault - Br) and by strike-slip faults on the north and the south. The Mölltal fault (Mö) bounds the southwestern margin while the the southeastern margin is limited by Austroalpine units. The northern margin is bounded by the Salzach-Ennstal-Mariazell-Puchberg (Se) fault (Frisch et al., 2000; Rosenberg et al., 2004), (Fig. 2.2).
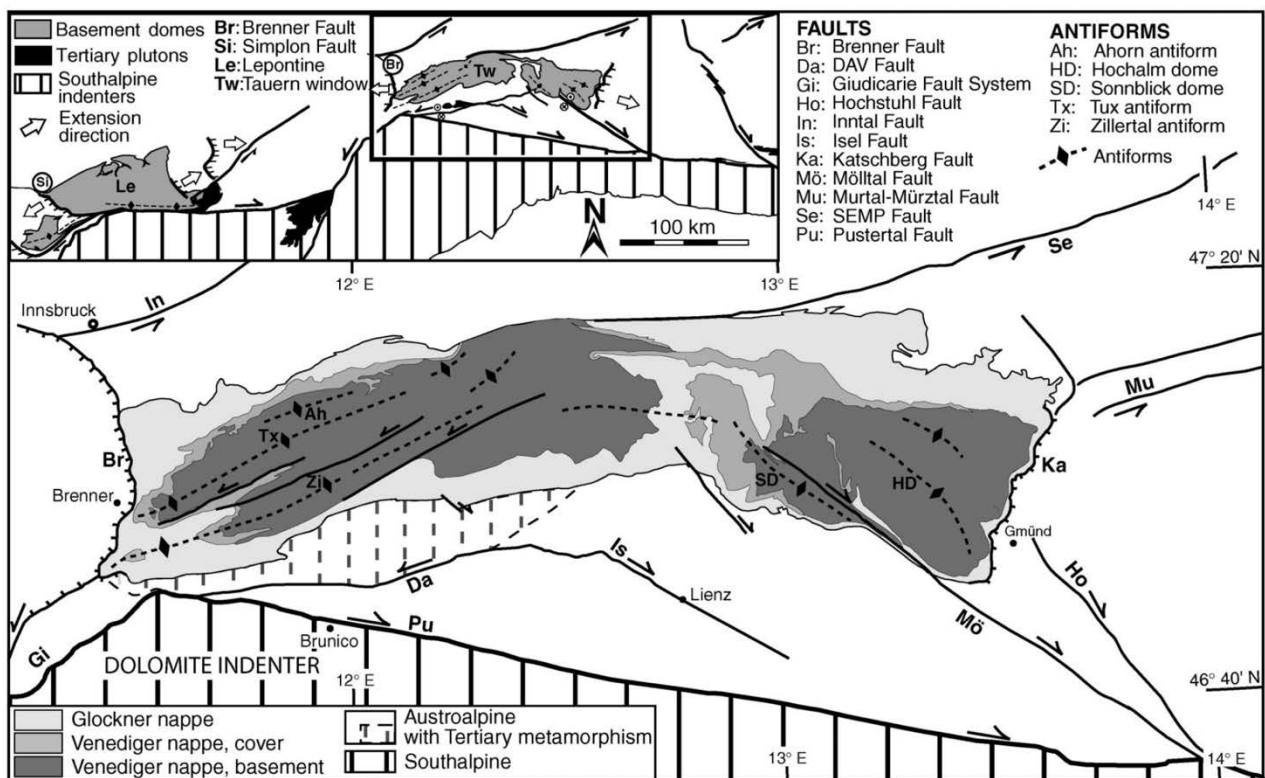

Fig. 2.2: Simplified tectonic map of the Tauern Window showing the bounding faults and the main tectonic units (Rosenberg et al., 2004).

The Tauern Window is a metamorphic dome that exposes rocks of the Penninic domain metamorphosed under greenschists- to amphibolite-facies conditions (Frisch et al., 2000; Rosenberg et al., 2004). A thin slice of eclogite-bluschist facies units is located at the center of the Tauern Window (Selverstone et al., 1984; Selverstone & Spear, 1985). The domal structure of the Tauern Window is the result of crustal-scale folding, coupled orogen-perpendicular shortening and orogen-

parallel extension (Rosenberg et al., 2004; Schmid et al., 2013) and a NNE directed indentation (Rosenberg et al., 2004). It is the largest tectonic window in the Alps and displays the most thickened ductile crust of all the Alps (Fig. 2.3) (Schmid et al., 2004; Rosenberg et al., 2004).
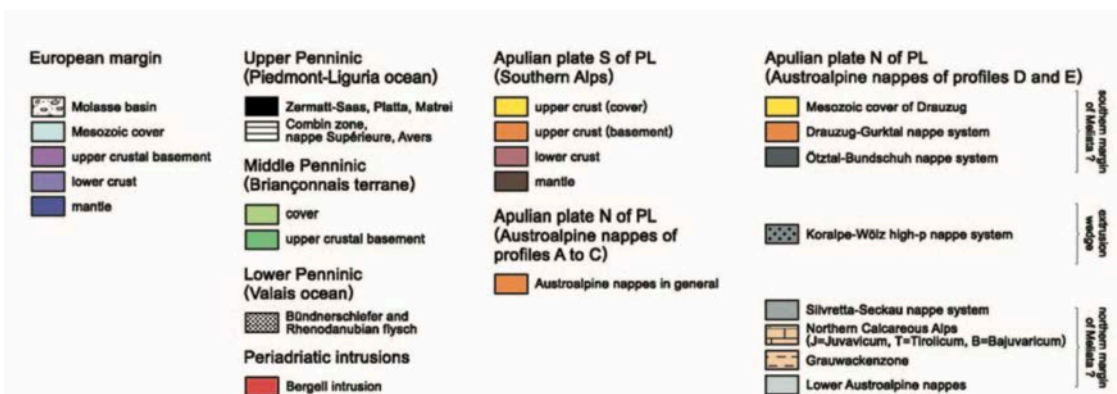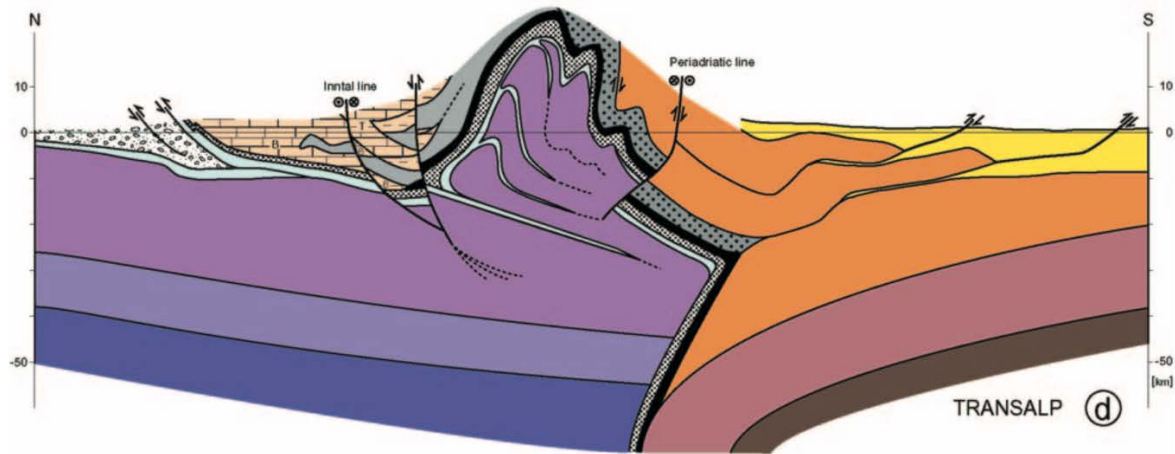

Fig. 2.3: TRANSALP transect cutting through the Tauern Window (Schmid et al., 2004). The orogen displays a strong thickening. Compiled with data from Schmid et al. (2003), Lippitsch (2002) and the Transalp Working Group (2003).

Selverstone (1985) proposed a subdivision of the western Tauern Window in three structural units: the Zentralgneise, the Lower Schieferhülle (LSH) and the Upper Schieferhülle (USH). Kurz et al. (1998), instead, proposed a more detailed description of the entire Tauern Window (Fig. 2.4). Following these authors, the lowest structural unit is the Venediger nappe complex that is overlain in turn by the Storz, the Rote Wand-Modereck and the Glockner nappe (Fig 2.4b).
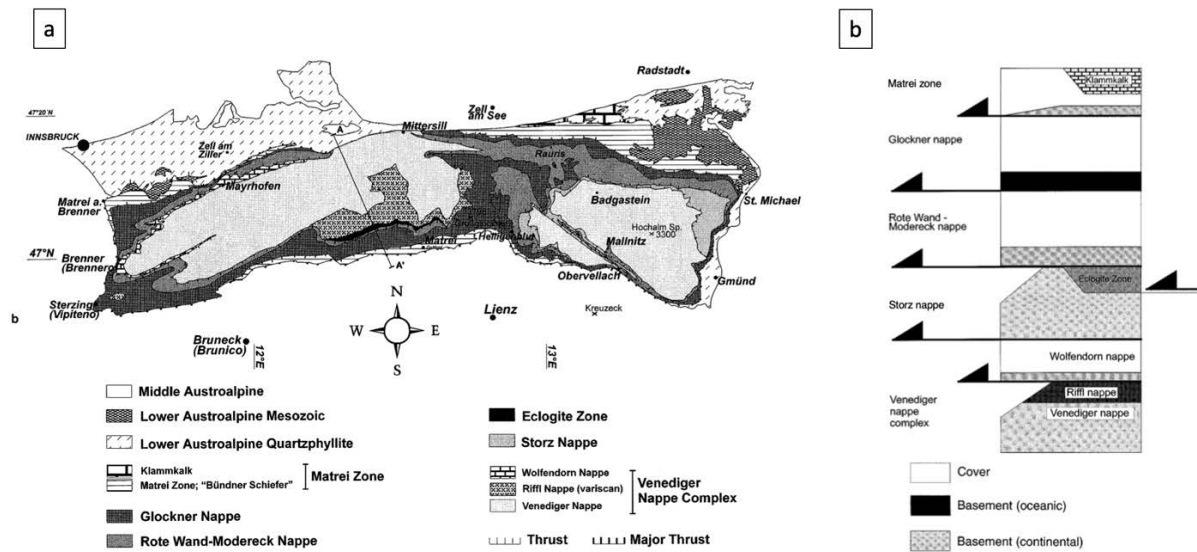
Fig. 2.4a and b: a) Tauern Window tectonic units as proposed by Kurz et al. (1998); b) Tauern Window tectonostratigraphy (Kurz et al., 1998).

The Venediger nappe (Fig. 2.5) is composed by basement rocks and metagranitoids overlain by younger metasedimentary covers. The basement consists of polymetamorphic rocks which underwent both the Variscan and the Alpine metamorphisms. It includes amphibolites, migmatites, micaschists and locally by serpentinites and pre-Alpine ophiolites (Kurz et al., 1998). These basement rocks were intruded by voluminous granitoids at 310-290 Ma (Kurz et al., 1998; Schmid et al. 2013). During the Alpine orogenesis the granitoids were metamorphosed into orthogneisses, and now form the Zentralgneise Auct. Complex. Three main gneiss bodies compose the Zentralgneise complex: the Ahorn Massif, the Tux Massif and the Zillertal-Venediger Massif (Finger et al., 1993). Above the aforementioned gneisses, a metasedimentary cover is found (Veselá & Lammerer, 2008). These Permo-Carboniferous and Mesozoic covers are clastic and volcanic in origin and were deposited in the Pfitsch-Mörchner Basin (Veselá & Lammerer, 2008).
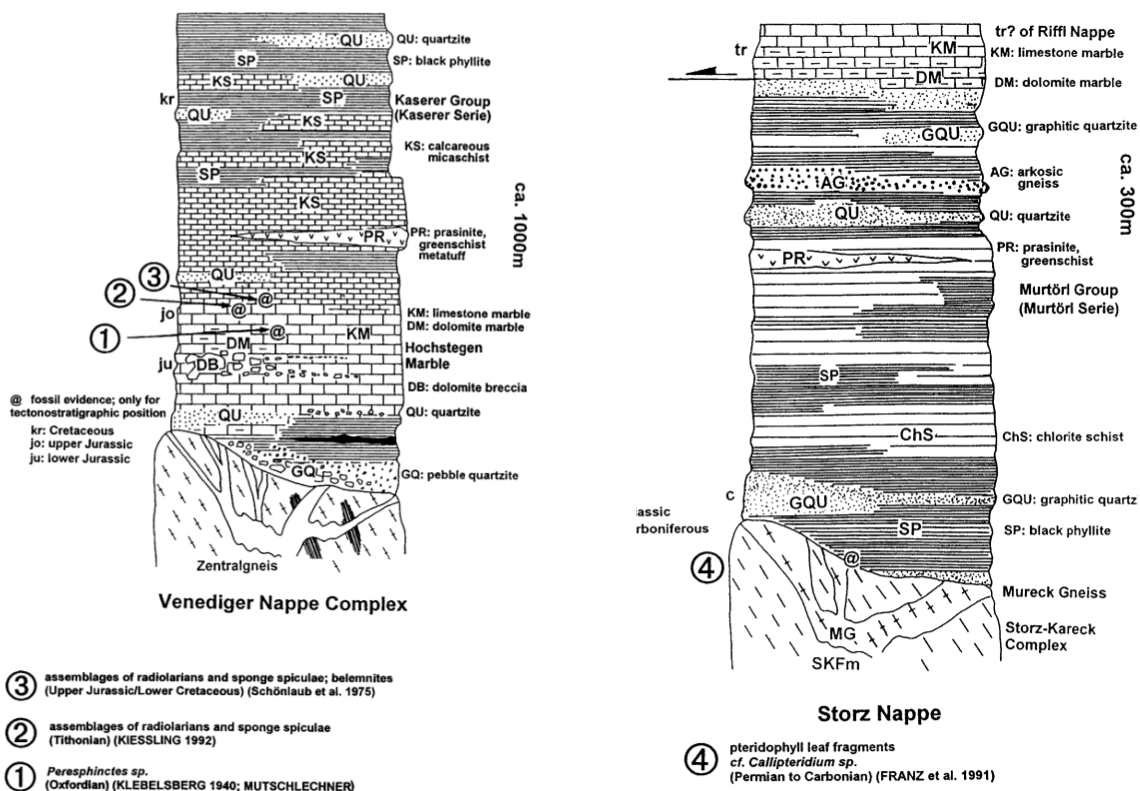
At higher structural levels, the Storz nappe (Fig. 2.5) is composed by amphibolites, albite gneisses, biotite-chlorite-epidote gneisses, chlorite-albite schists and metagabbros, and takes the name of Storz-Kareck Complex (Exner et al., 1971). The complex units are intruded by a former pre-Variscan granitoid now forming the Mureck gneiss. The whole basement sequence is covered by a metasedimentary sequence that consists of black phyllites and micaschists, graphitic quartzites, chlorite-chloritoid schists, arkosic gneisses and minor prasinites (Exner et al., 1971). The Storz nappe shares the same structural position as the Eclogite Zone (Fig 2.5). The eclogite protoliths are tholeiitic basalts and gabbros (Miller et al., 1979). Metagabbros lenses are intercalated with metasediments

such as quartzites, paragneisses, garnet-micaschists and calcitic and dolomitic marbles. Eclogites are usually retrogressed to garnet-amphibolites and garnet-greenschists (Miller et al., 1979).

The Rote Wande-Modereck nappe is located above the Storz nappe (Fig. 2.5). The nappe is mainly composed by basement slices and paragneisses from the metasedimentary quartzites, marbles and greenschists units that form the cover (Exner et al., 1964).

The Glockner nappe represent a former ophiolitic sequence and is found on top of the Rote Wande-Modereck nappe (Fig 2.4b). The base of the Glockner nappe consists of serpentinites and ultramafic rocks covered by a sequence of meta cherts, quartzites, calcitic marbles, calcareous schists and less often garnet amphibolite and strongly retrogressed eclogites intercalated with greenschist and amphibolites (Höck, 1983).

The highest structural units, tectonically juxtaposed to the Austroalpine basement, are the Matrei zone and the Klammkalk zone (Fig 2.4b). The Matrei zone consists of a metamorphic flysch of calcareous and carbonate-free micaschists, breccias and olistolites (Frisch & Raab, 1987). The presence of repeated thrusts makes serpentinites and Austroalpines rocks to be found in between the meta-flysch. The Klammkalk zone is instead constituted by calcschists, marbles and green phyllites that are considered as olistoliths of Austroalpine provenance (Exner, 1979).

Venediger Nappe Complex

③ assemblages of radiolarians and sponge spiculae; belemnites
(Upper Jurassic/Lower Cretaceous) (Schönlaub et al. 1975)

② assemblages of radiolarians and sponge spiculae
(Tithonian) (KIESSLING 1992)

① *Peresphinctes sp.*
(Oxfordian) (KLEBELSBERG 1940; MUTSCHLECHNER)

Storz Nappe

④ pteridophyll leaf fragments
cf. *Callipteridium sp.*
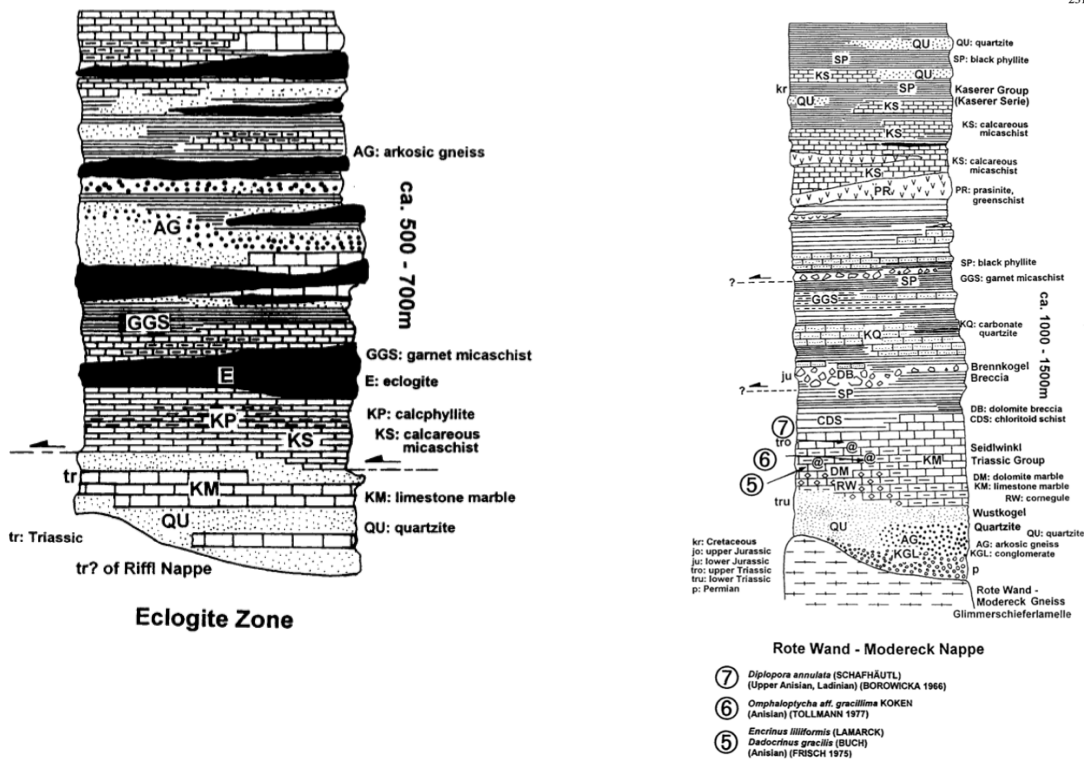(Permian to Carbonian) (FRANZ et al. 1991)

Fig. 2.5: Stratigraphy of the Venediger nappe (top left), Storz Nappe (top right), Eclogite zone (bottom left) and Rote Wand-Modereck nappe (bottom right), after Kurz et al. (1998).

2.2 The SW Tauern Window in the Valle di Vizze

The Valle di Vizze (Pfitschtal), where the rocks studied in this thesis were collected, is located in Northern Italy, at the border with Austria. Geologically, the valley is included in the south-western Tauern Window.

The large-scale structure of the NW TW is composed by a sequence of two tight east-west oriented antiforms, also called the Venediger Duplex (Fig. 2.6; Lammerer et al., 2008). The northern antiform exposes the Tux orthogneisses and the southern antiform exposes the Zillertal orthogneisses. The Vizze (or Greiner) synform is located in between the two anticlines.
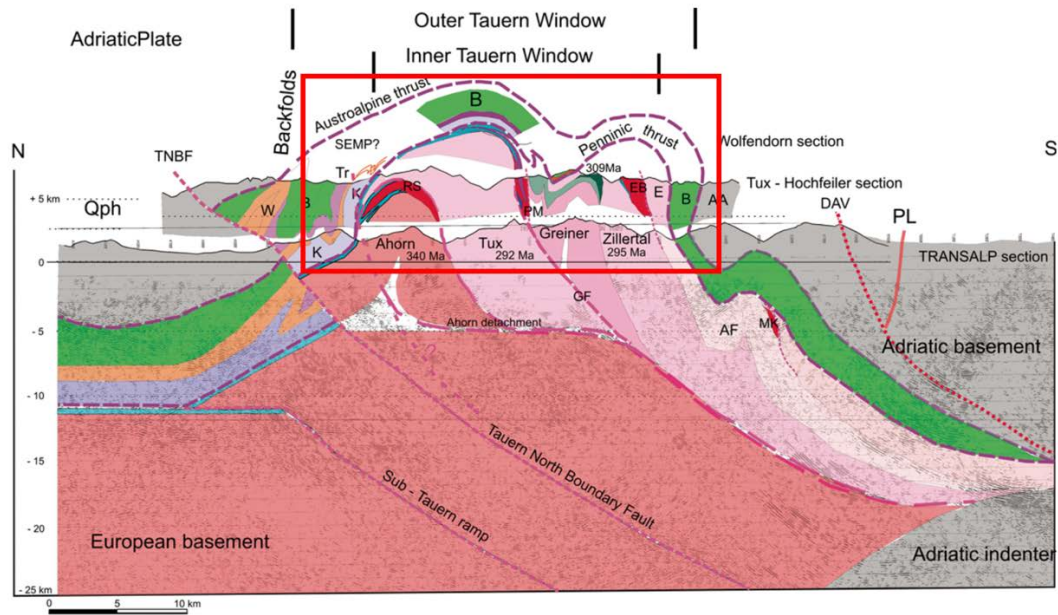
Fig 2.6: Cross-section through the SW Tauern Window, modified after Lammerer et al. (2011). The red box highlights the anticlines of the Venediger Duplex. Legend: Qph—Quartzphyllite zone; W—Wustkogel series; B—Bündner schists; Tr—Middle Triassic carbonates; K—Kaserer series (Devonian–Carboniferous colored mélange); RS—Riffler-Schönach clastic basin; PM—Pfitsch-Mörchner clastic basin; EB—Eisbrugg clastic basin, E—Eisbrugg gneiss nappe; AF—Ahrntal fault; MK—Maurerkees basin; AA—Australpine south of the Tauern Window; TNBF—Tauern North Boundary Fault; SEMP—Salzach-Ennstal-Mariazell- Puchberg Fault; Sub-TR—Sub Tauern Ramp; DAV—Defereggen-Antholz-Vals Fault.

Within the synform, metasedimentary rocks belonging to the Pfitsch-Morchner Basin (Fig. 2.7; Veselá and Lammerer, 2008; Franz et al., 2021) are exposed. These rocks are the post-Variscan cover that overlies the Zentralgneis complex and are divided into the Modereck, Wolfendron, Pfitsch and Greiner units. This sequence is the so-called Lower Schieferhülle (De Vecchi & Baggio, 1982) and composes part of the Venediger Duplex (Lammerer et al., 2008). Some calcschists and metabasites of the Glockner nappe are outcropping at the top of the synform and are also referred to as Upper Schieferhülle.

Veselá and Lammerer (2008), carefully described the metasedimentary units of the Pfitsch-Mörchner Basin. The Modereck unit is composed by calcitic and dolomitic marbles, paragneisses, micaschists, quartzites and a carniola level. The Wolfendron unit instead, is a combination of Zentralgneise slices and metasedimentary rocks. The main lithologies are paragneisses, metaconglomerates, kyanite-bearing quartzites (Rhaetizit quarzit Auct.) and calcitic and dolomitic marbles. The Pfitsch unit is divided in three formations: the Vizze Fm. (metaconglomerates, metarhyolites and paragneisses), the Windtal Fm. (lazulite-kyanite-sericite quartzites) and the Aigerbach Fm. (calcitic and dolomitic marbles with a basal evaporitic level) (Fig. 2.8). Finally, the Greiner unit consists in garnet

micaschists, the Garbenschiefer Auct. (garnet-amphibole micaschists with sheaf-shaped amphibole crystals up to 5-6 cm of length) and the Furtschaglschiefer Auct. (graphitic garnet-biotite micaschists).

The Furtschaglschiefer Auct., also named Greiner Schist, is the main subject of this thesis and I will focus on its formation and its tectonometamorphic history.

The Furschtaglschiefer unit derives from a pelitic protolith of Permo-Carbonferous age (Veselá & Lammerer, 2009) that probably escaped the Variscan metamorphism and was metamorphosed under lower amphibolite facies conditions only during the Alpine orogenesis (Hoernes & Friedrichsen, 1974).
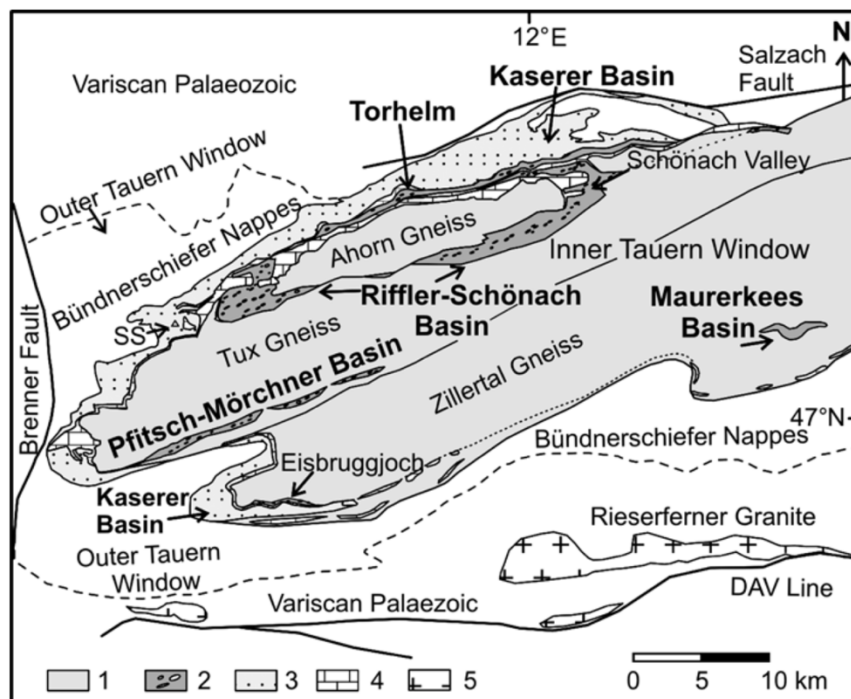

Fig. 2.7: Pfitsch-Mörchner Basin position in the western Tauern Window (Veselá and Lammerer, 2008 modified after Veselá et al., 2008).
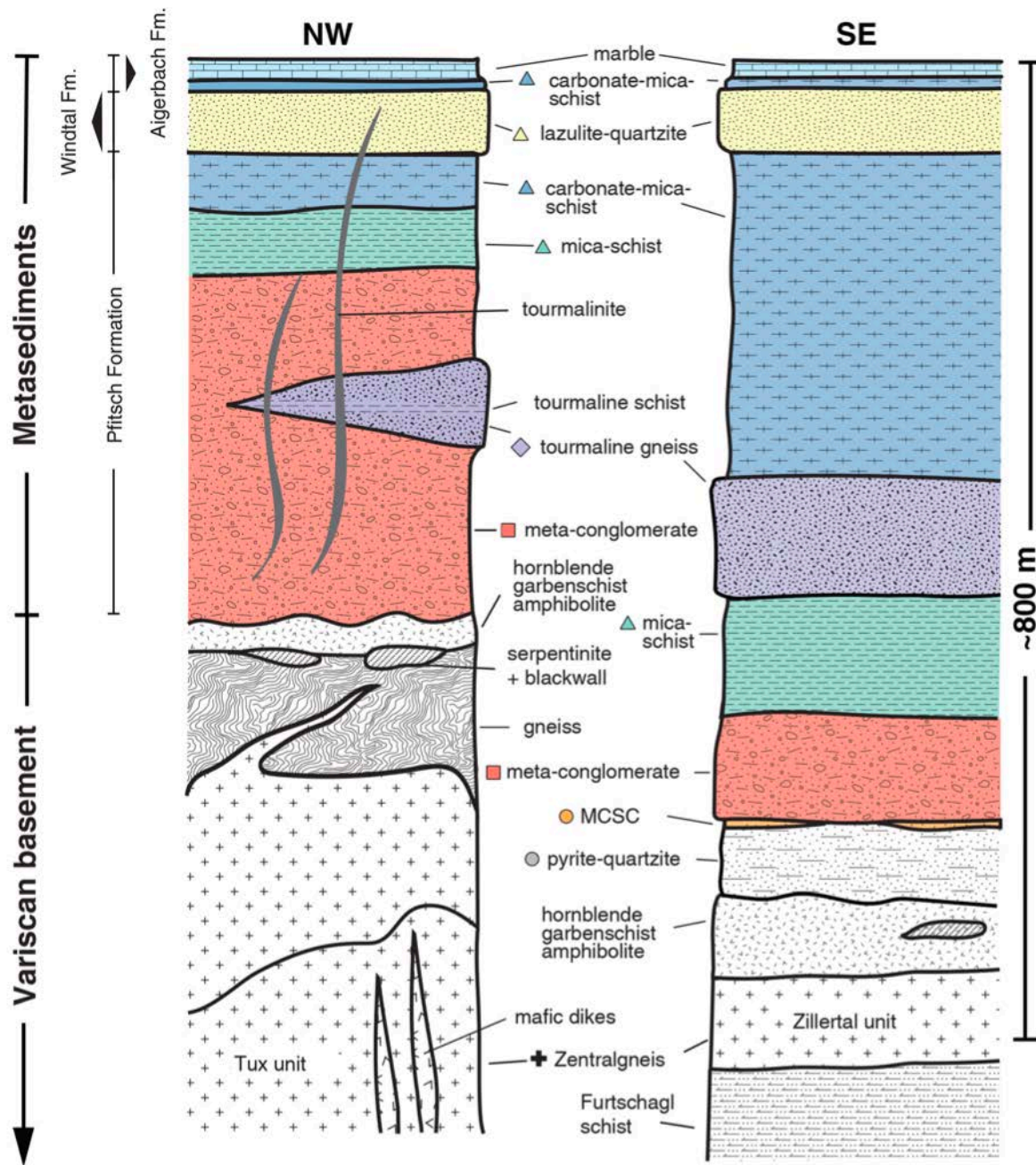
Fig 2.8: Pfitsch-Mörchner Basin metasedimetary sequence and Variscan basement rocks (Franz et al., 2021).

Da Mommio (2018, PhD thesis), recognized three separate Alpine deformation phases. The D3 deformation phase is the youngest phase and is related to the folding events that formed the big-scale anticlines of the Venediger Duplex and it is, in fact, characterized by big low-angle WSW-WNW dipping open folds. No axial plane foliations are developed during the D3 phase, but only in phyllosilicate-rich lithologies. D3 structures overprint D2 structures and the associated pervasive S2 axial plane foliation. The D2 deformation phase is syn-metamorphic and the S2 foliation is defined

by greenschists and amphibolite facies minerals. The S1 foliation is still preserved inside fold hinges and thus the main foliation must be considered as a S1+S2. Finally, the D1 deformation phase is associated with the S1 foliation that is rarely preserved. In between the D2 and D3 deformation phases, the so-called "Tauernkristallisation" took place (Sander, 1912). This was considered a Barrovian-style static metamorphic phase during which the rock reached amphibolite facies metamorphism with the formation of amphibole, biotite, staurolite and kyanite. Following studies, including this thesis, clearly showed that the amphibolite-facies metamorphism in many units of the SW Tauern Window is syntectonic.

Hoernes and Friedrichsen (1974), and the subsequent work of Friedrichsen and Morteani (1978), were the first authors to estimate the temperatures reached during the Alpine Barrovian metamorphism in the Western Tauern Window. Their temperature reconstruction shows a concentric isotherm distribution with an external zone ranging from 400°C to 550°C and an internal zone reaching temperatures of 600-650 °C (Fig. 2.9).
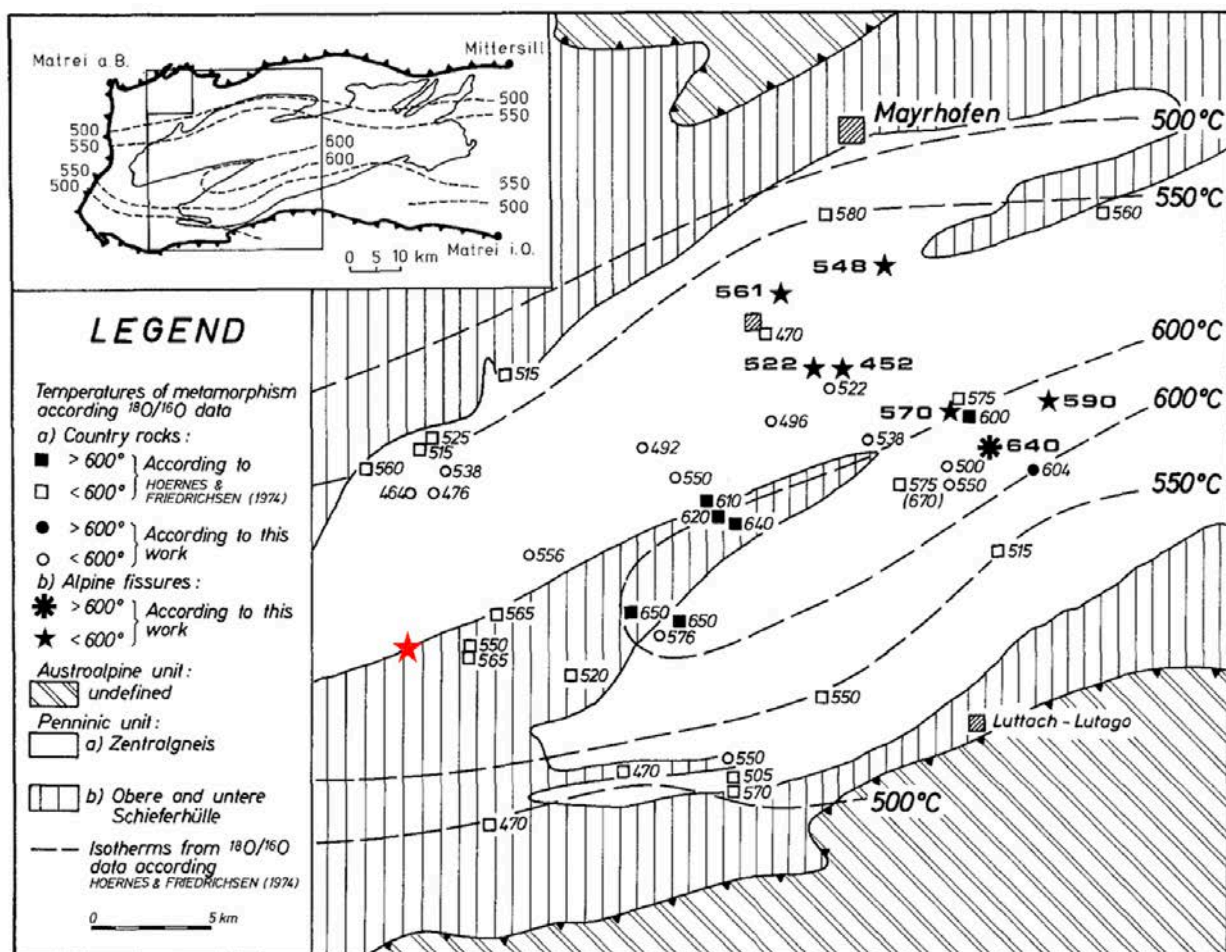

Fig. 2.9: Temperature distribution during the Alpine metamorphism (modified after Friedrischen and Morteani, 1978). The red star indicates the sample location.

To date, the metamorphic history of the Tauern Window has been better constrained. In the western TW, Selverstone et al. (1984) and Selverstone and Spear (1985) estimated the metamorphic conditions for the LSH (Fig. 2.10) and the USH (Fig. 2.10), respectively. The LSH has first experienced an high-pressure phase with temperatures of 495-545°C and pressures of 0.9-1 GPa, followed by a decompression phases with temperature of 525-575°C and pressure of 0.7 GPa (Selverstone et al., 1984). The USH followed a similar PT path with a first phase at 0.7-0.8 GPa, then a prograde phase with temperatures of up to 500°C and pressure of 0.75 GPa, and finally a decompression phase down to lower greenschist facies.
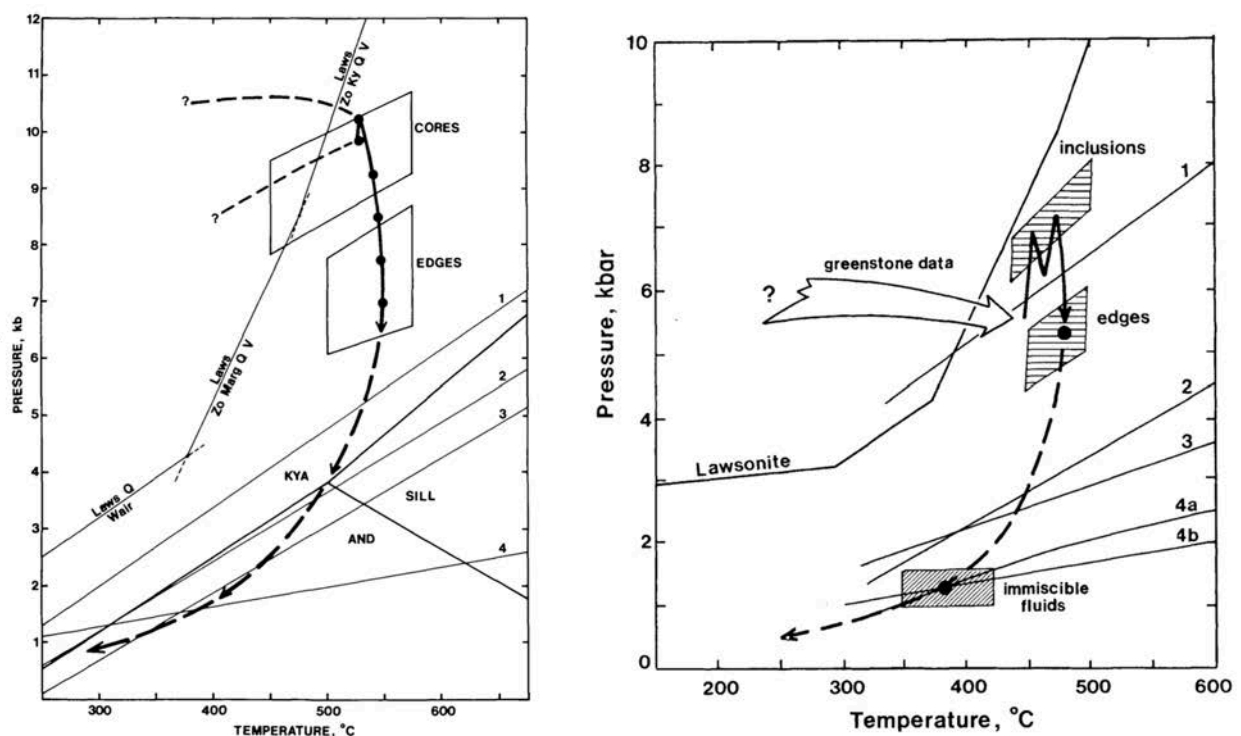

Fig. 2.10: LSH (left) and USH (right) P-T paths (Selverstone et al., 1984; Selverstone and Spear, 1985).

Despite the extensive work on the metamorphic conditions, not much has been done to constrain the age of metamorphism in the SW Tauern Window. Christensen et al. (1994) estimated the age of the high temperature phase at 30 ($\pm$ 2) Ma when garnet in both the LSH and the USH stopped growing. Garnet growth in the LSH started at 62.5 ($\pm$ 1.5) Ma, suggesting that the high pressure phase had already started. A following work by Cesare et al. (2001) argues that Alpine metamorphism may be 10 Ma younger from $^{206}Pb/^{238}U$ ages on zircons.

2.3) Sampling

The Furtschaglschiefer unit is well exposed in a ENE directed fold that is the synform of the Venediger Duplex. These rocks crop out along the road from San Giacomo to Passo di Vizze, where sometimes some outcrops of Garbenschiefer are also present. The Furtschaglschiefer is also exposed and has been sampled near the village of Sasso (Stein) along two stream cuts (Fig. 2.11).
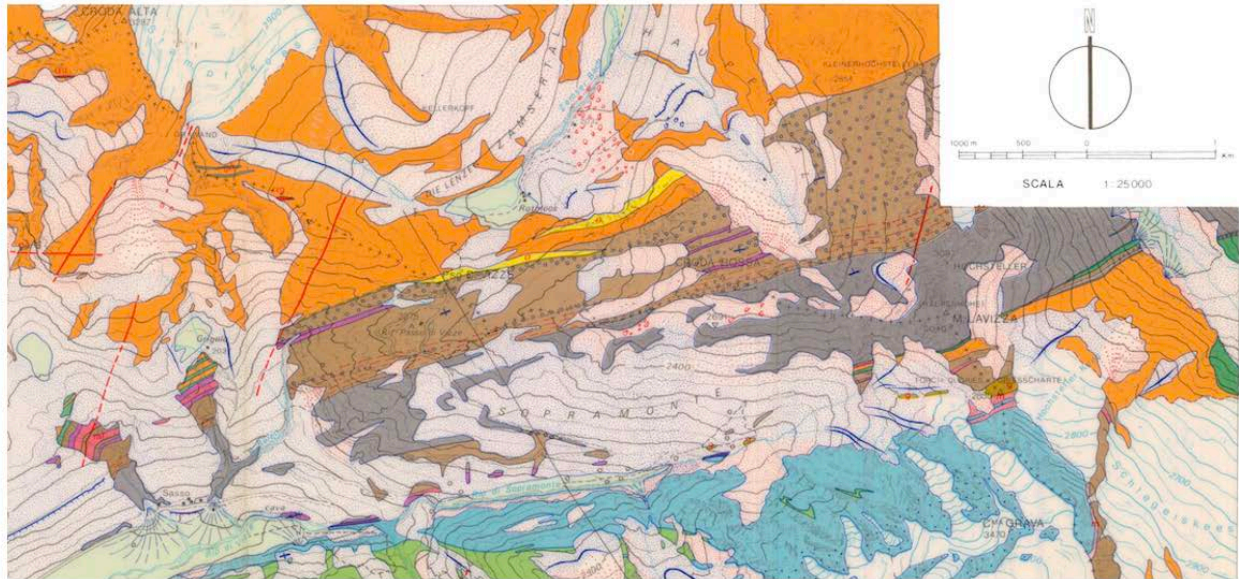

Fig. 2.11 Furtschaglschiefer band (grey color). Extract of the Valle di Vizze geological map from Baggio et al. (1975). The Furtschaglschiefer is described as "graphitic garnet-phyllites and micaschists". Legend: Pink - Hochgestein Auct. (marbles); Purple – quartzites; Brown – sandstone gneisses and conglomeratic gneisses; Green – amphibolitic gneisses; Orange – Tux gneisses; Dark orange and green – leucocratic gneisses and dioritic/gabbrodioritic gneisses; Yellow – serpentinites; Light blue and light green- calcschists and dolomitic marbles.

The main aim of the sampling was to collect the less altered samples in order to avoid any alteration of biotite for our microstructural analysis. On the field, we realized that the Furtschaglschiefer unit shows alternating dark and light layers depending on the mineralogy and the graphite content (see Chapter 4). During the sampling, we privileged darker bands, even though some of the lighter ones have been collected.

Samples have been collected from six different outcrops: four (VIZ01/VIZ02, VIZ03, VIZ04, VIZ05) along the road towards the Passo di Vizze, while other two rocks (VIZ06, VIZ07) come from the outcrops near Stein (Sasso) (Fig. 2.12; Tab 2.1). Samples VIZ01 to VIZ05 have been all collected on

bedrock, instead samples VIZ06 and VIZ07 have been collected from blocks or boulders along streams.
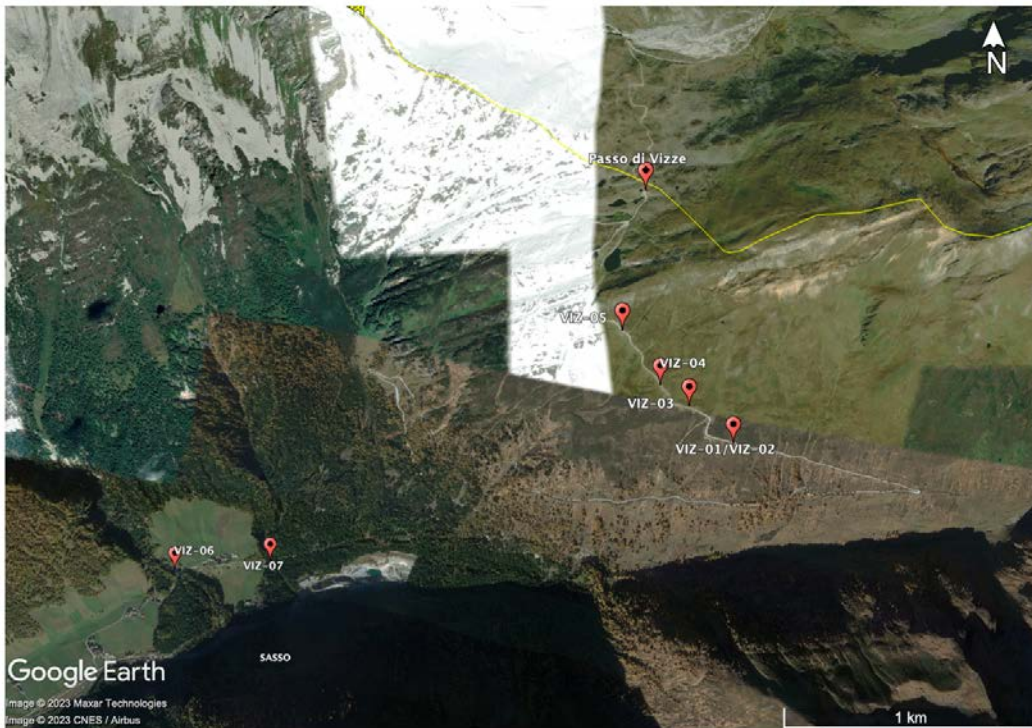

Fig 2.12: Sampling locations.

Samples	Coordinates
VIZ01/VIZ02	N 46°59'07.3'' E 11°39'52.5''
VIZ03	N 46°59'11.8'' E 11°39'46.8''
VIZ04	N 46°59'14.7'' E 11°39'40.9''
VIZ05	N 46°59'22.2'' E 11°39'33.1''
VIZ06	N 46°58'59.0'' E 11°37'16.0''
VIZ07	N 46°58'46.2'' E 11°38'14.0'

Tab 2.1: Sample coordinates.

3 Methods

3.1 Optical microscopy

Optical microscopy has been applied in order to recognize the mineral phases and the microstructural settings present in the samples and to measure microstructural parameters of biotite porphyroblasts such as aspect ratio, boudin lengths and porphyroblasts orientation. Detailed petrographic observations have been performed with polarized-light optical microscopes at the Department of Geosciences on oriented thin sections (30 microns) that have been cut perpendicular to the foliation and both parallel and normal to the lineation.

High resolution thin section scans (20x) and microstructural measurements (aspect ratio, boudin length, porphyroblasts orientations) have been acquired with a scanning stage polarized-light optical microscope at ETH Zürich.

3.2 Scanning Electron Microscopy

Scanning Electron Microscopy (SEM) and Energy Dispersive Spectroscopy (EDS) investigations were aimed at the recognition of eventual additional mineral phases and at the identification of the mineral chemistry of the investigated phases.

SEM analysis has been performed with the Dual beam FIB-FE-SEM Tescan SOLARIS of the Department of Geosciences. Images have been acquired with a working distance of 4 mm and an acceleration voltage of 5 and 10 keV.

3.3 Micro X-ray Computed Tomography

Micro X-ray Computed Tomography (µCT) analysis is a powerful tool in the reconstruction of rock microstructures and microfabrics. This technique has been applied to retrieve the 3D geometry of the porphyroblasts in the rock (Ketcham, 2005; Cnudde & Boone, 2013; Sayab et al., 2015; Sayab et al., 2021). The analysis has been performed on a 2x1x3 cm rock volume at the University of Leeds by Dr. Alice Macente.

A Zeiss Versa 410 X-ray Computed Tomography system has been used to perform the scans. The instrument is equipped with an X-ray source-voltage range of 40-150 kV and a maximum power of 30 W.-XCT were acquired with a 0.4 X optical lense, a voltage of 130 kV and a power of 12 W. 2401 projections were acquired over 360° rotation, with an exposure time of 5 seconds per frame. An HE1

filter was used to improve transmission values. No frame averaging was needed. Data were then reconstructed using Zeiss proprietary software. The final reconstructed pixel size was 12.73 microns. Image analysis of the mineral phases has been performed using the software Thermo Scientific™ Amira-Avizo™ Avizo 3D v. 2022.2. From an initial grey-scale image, the image is filtered for denoising, and then segmented with a watershed algorithm to obtain the separated phases. In image processing, the watershed algorithm treats the different gray scale values as different height and computes the lines running along the tops of the ridges (Romero-Zaliz & Reinoso-Gordo, 2018). Then, the image is post-processed to remove artifacts or unwanted particles (for a more accurate description, see Chapter 4).

4 Results

4.1 Field observations

In the field, the *Furtschaglschiefer* unit is dark grey in color with lighter intercalations (Fig 4.1). The whole rock mass is foliated, lineated and folded, reflecting the strong deformation associated woth. Alpine metamorphism. Structural measurements collected from different outcrops along the whole area of the unit show a NNE-SSW foliation dipping at an average of 340N and a dip angle of 60°, and an E-W lineation with an average trend of 265N and a plunge of 20° (Fig 4.2). The measured directions and some plurimetric minor isoclinal fold observed in the unit that show an average dip of 340N and a dip angle of 80°. (Fig 4.3, Fig 4.4) are consistent with the large-scale fold system direction (Fig 2.6).

Fig. 4.1: Furtschaglschiefer outcrop showing the alternating dark and light layer.
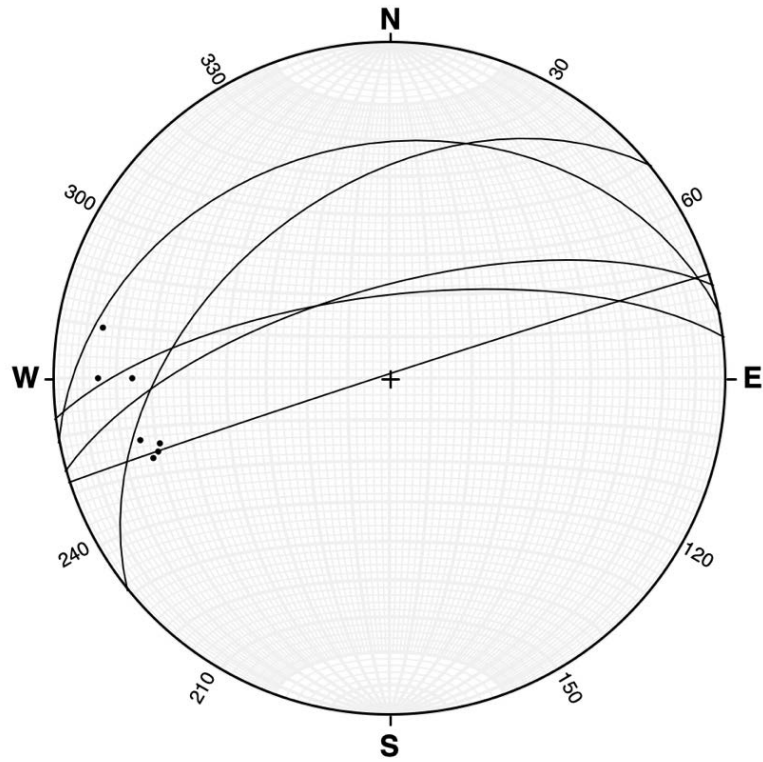
Fig 4.2: Lower hemisphere stereonet projection of the structural measurements. The Furtschaglschiefer unit shows a NNE-SSW dipping foliation and an E-W lineation.

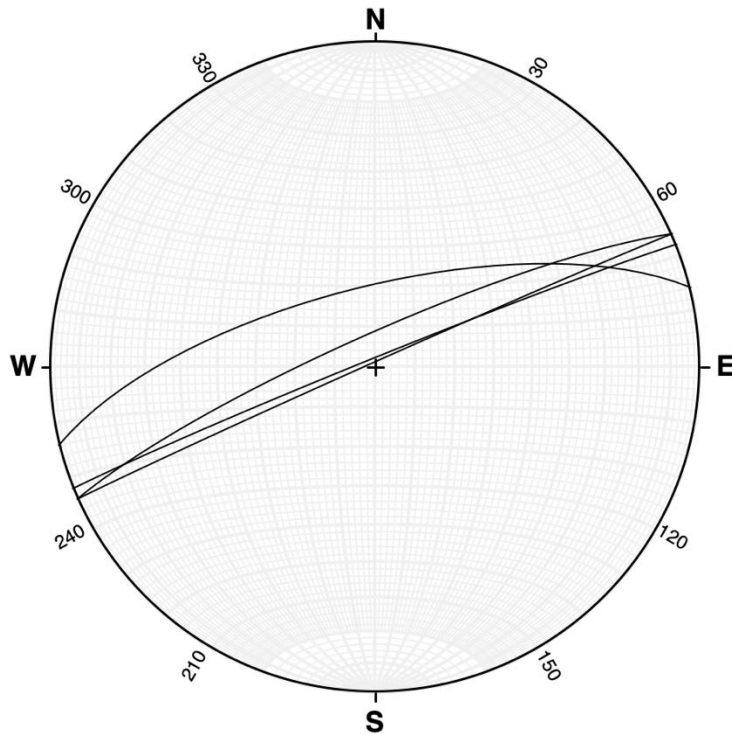Fig. 4.3: Minor folds in the Furtschaglschiefer unit.

Fig 4.4: Lower hemisphere stereonet projection of the structural measurements of the axial planes of the minor folds.

Dark and light layers are irregularly alternating with a maximum thickness of 20-30 cm and display macroscopic differences in composition and appearance (Fig. 4.5) with the darker layers that are usually strongly foliated and lineated with abundant garnet and biotite, while the lighter layers are more compact and show little to no garnet and less biotite than the darker layers (Fig. 4.5).

Fig. 4.5: Schistose dark layer and more massive light layer of the Furtschaglschiefer unit.

From the macroscopic point of view, garnet (up to 2 mm; rarely up to 1 cm), and biotite porphyroblasts (up to 1 cm) are observed, particularly in the darker layers (Fig.4.6). Microboudinaged biotites and the related biotite and quartz increments are clearly visible at the hand sample scale; also, the lineation is clearly evident due to the alignment of elongate biotite porphyroblasts (Fig 4.6).

Fig. 4.6: Macroscopic appearance of the dark layers. Garnet porphyroblasts are visible in the hand sample as well as biotite and the lineation that it defines.

4.2 Petrographic observations

Petrographic observations have been mainly performed on thin sections cut parallel to the lineation, due to the fact that the lineation itself formed when biotite deformed and aligned. Using thin sections parallel to the lineations allows to better observe the microboudinage microstructures.

The representative *Furtschaglschiefer* assemblage is the one of the dark grey layers. The mineral assemblage is characterized by biotite (Bt), garnet (Grt), ilmenite (Ilm), quartz (Qz), chlorite (Chl), plagioclase (Pl), muscovite (Ms), graphite (Gr), zircon (Zrn) and apatite (Ap) (mineral abbreviations after Whitney and Evans, 2010). Epidote (Ep) is commonly found in some samples while staurolite (St) and amphiboles are very rare and have been observed in one sample each. This paragenesis corresponds to the transition between upper greenschist- and lower amphibolite-facies conditions. This definition is possible thanks to the presence of the typical greenschist facies chlorite that is still stable in the sample, and also by the rare staurolite crystals that are typical of the amphibolite facies. The foliation is evident at the thin section scale and is clearly defined by phyllosilicates. Muscovite and chlorite are the principal components defining the foliation. Some elongated biotites (type III, see section 4.2.1) define the foliation as well. The microstructure as a whole is characterized by the

ubiquitous presence of graphite that further highlights the foliation and is frequently found as inclusion in biotite and garnet porphyroblasts.

The whole anisotropy is plane-parallel with only minor deflections related to the anastomosing around porphyroblasts, and no oblique fabrics such as crenulations or S/C fabric have been observed.
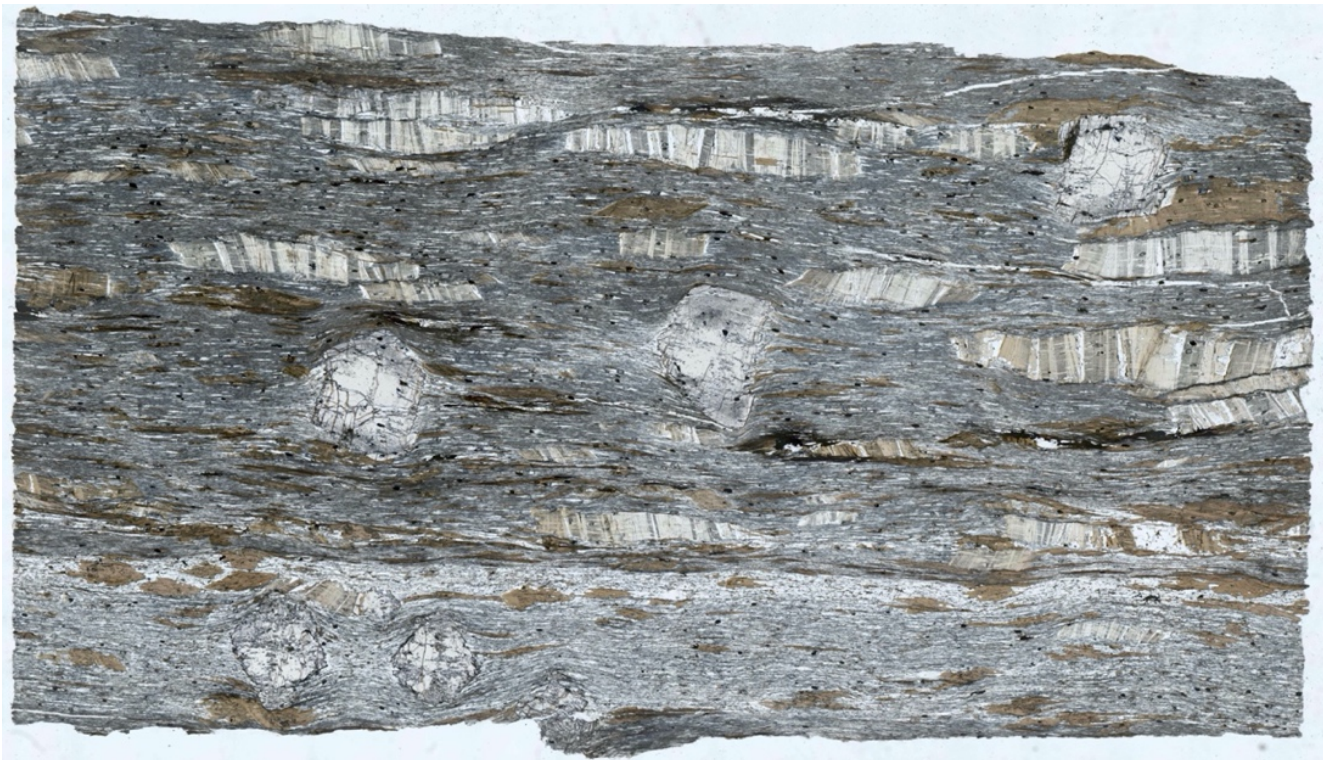

Fig 4.7: Plane polarized light (PPL) thin section scan of sample VIZ01-6P.

As seen in the hand samples, the porphyroblasts are biotite and garnet, with the addition of ilmenite which is only visible at the thin section scale (Fig 4.8). The foliated matrix is mainly composed of quartz, chlorite, muscovite, plagioclase and graphite (Fig. 4.9). Chlorite is stable inside the matrix and is pale green in color (Fig. 4.10), suggesting the presence of a Mg-rich chlorite. Phyllosilicates are very similar in color due to the fine-grained matrix and hence it is difficult to discriminate them under plane polarized light (PPL). Due to the fine-grained matrix and the intimate association of chlorite and muscovite, the latter appears pale green (Fig 4.10).

The accessory minerals are epidote, zircon, tourmaline and apatite. Rare staurolite crystals have been observed at the edges of garnet in one sample (Fig 4.11).

Even though epidote has been defined as an accessory phase, it is an important mineral even if its presence in the sample is discontinuous. When epidote is present, it is usually found in euhedral prismatic crystals (Fig. 4.12).

The lighter layers are characterized by a simpler mineral assemblage that is mainly constituted by coarser quartz, fine grained biotite and the same accessory minerals as the darker layer (Fig. 4.13). Carbonates are found in some samples (Fig. 4.14). Biotite is also forming pseudomorphs after amphibole in some samples (Fig. 4.15).
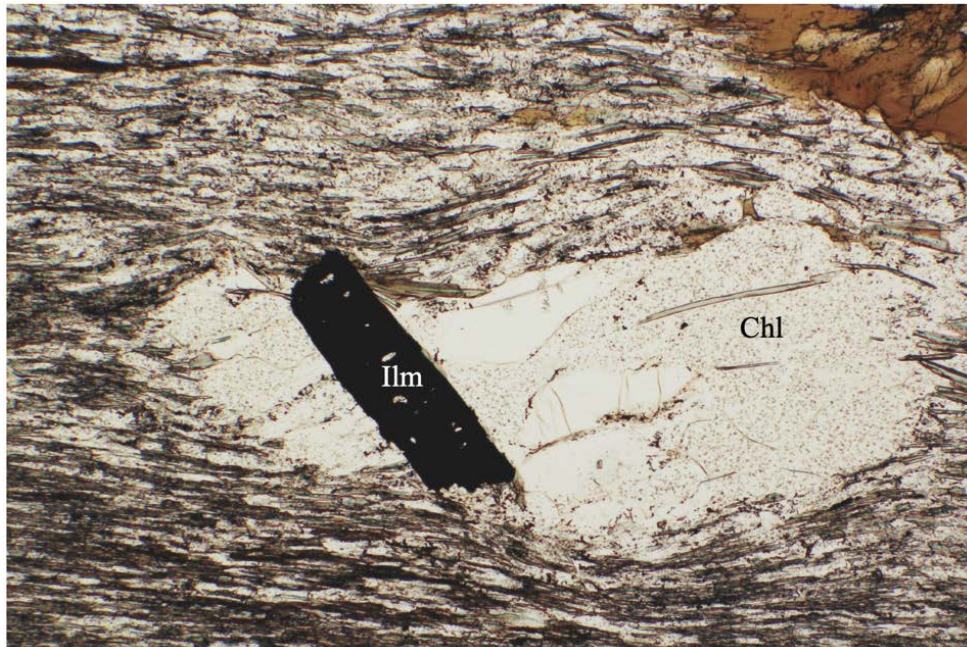

Fig. 4.8: Ilmenite porphyroblast with coarse quartz strain shadow containing also Mg-rich chlorite. The base of the photo is 5.3 mm long.
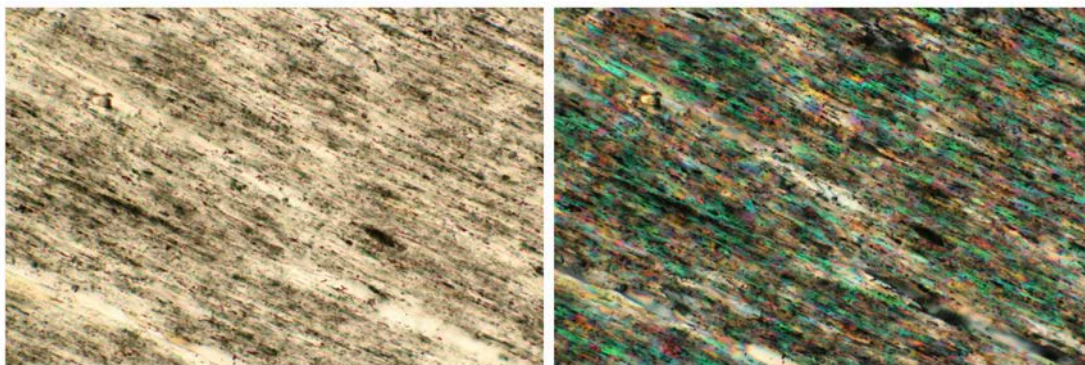

Fig. 4.9: Typical appearance of the matrix from the dark layers under PPL (left) and cross polarized light (XPL). The fine-grained assemblage is composed of quartz, plagioclase, muscovite and chlorite. The base of the photo is 0.68 mm long.
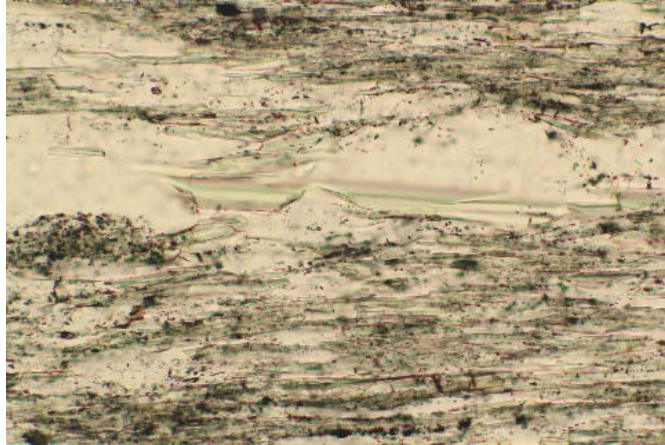
Fig. 4.10: Pale green muscovite in the dark layer matrix under PPL. The base of the photo is 0.68 mm long.

4.11: Staurolite crystals near the edge of a garnet (bottom) under PPL. The base of the photo is 0.68 mm long.
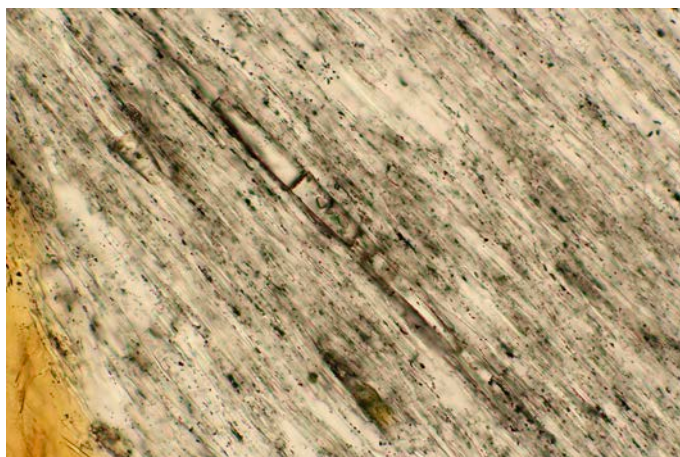

Fig 4.12: prismatic epidote crystal under PPL. The base of the photo is 0.68 mm long.
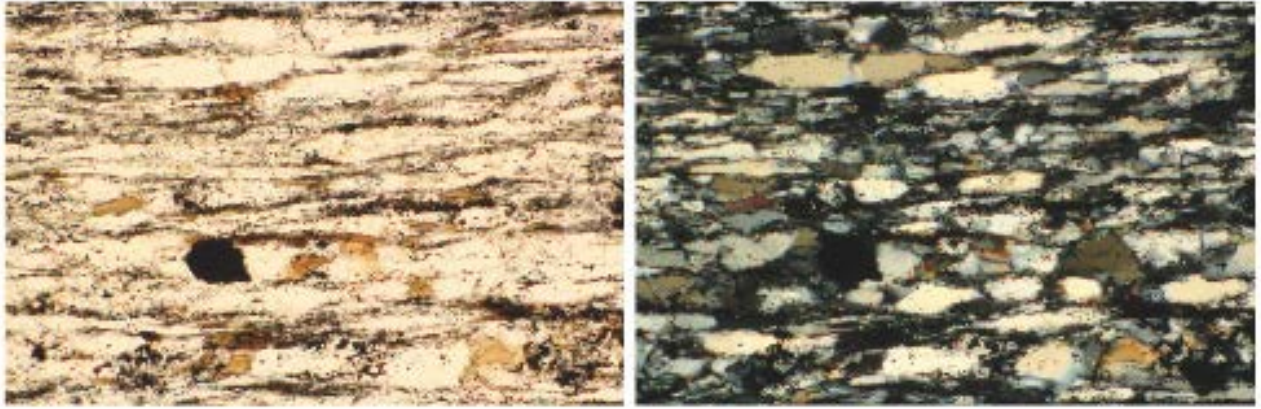
Fig. 4.13: Light layer composition with coarse quartz and fine biotite grains under PPL (left) and XPL (right). The base of the photo is 2.65 mm long.

Fig 4.14: carbonate crystals under PPL in sample VIZ07-5P. The black bar is 1 mm long.

Fig 4.15: breakdown structure under PPL of amphibole into biotite in sample VIZ07-5P. The black bar is 1 mm long.

4.2.1 Biotite

Biotite appears in three main microstructural types: the "foliation-perpendicular" microboudinaged biotites, the fanned *mica-fish* biotites and the foliation-parallel elongate biotites (Fig. 4.16). The microboudinaged biotites (hereafter type I) are the coarser in size (up to 1 cm in length), and typically show alternating graphite-rich and graphite-free sectors sometimes separated by quartz crystals coarser than those in the matrix, with some crystals of 0.7 mm in length (Fig. 4.17). These sectors, as well as biotite cleavage planes, are perpendicular to the foliation, while the graphite inclusions are parallel to it. Fanned biotites (type II) are smaller than the microboudinaged biotites with lengths of up to 3-4 mm and show both dextral and sinistral shear senses. The two shear senses are equally represented in the samples and, in fact 52 dextral and 41 sinistral porphyroblasts have been counted (Fig. 4.18). Finally, the elongated biotites (type III) show foliation-parallel cleavage planes and shapes and display similar sizes as the fanned biotites with lengths of 3-4 mm. In some cases, foliation-parallel biotite occurs within foliation-perpendicular biotite and seems to be mainly euhedral in shape (Fig. 4.19).

Graphite-rich sectors in microboudinaged biotites are characterized by faint intergrowths of alternating biotite and chlorite as opposed to graphite-free sectors that are composed of biotite only.

Biotite and chlorite are clearly grown together over graphite including it, meaning that chlorite is not formed during boudinage (Fig. 4.20).

Orientation measurements on 51 porphyroblasts shows that all types of biotite porphyroblasts share the same orientation of the long axis with respect to the foliation spanning from 353° to 10°, and thus exhibiting a range of ±10° of variability (Fig 4.21).
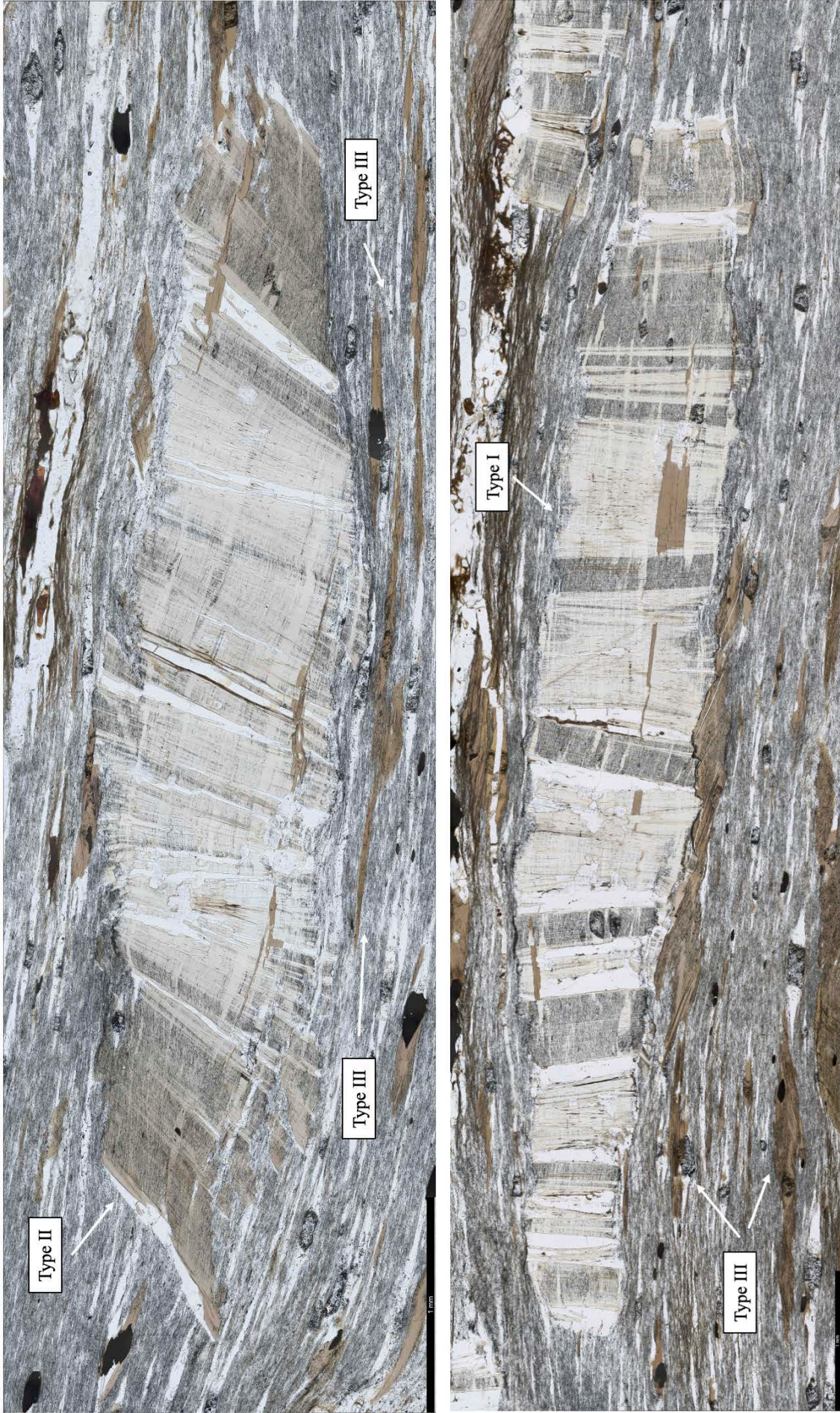
Fig. 4.16: the three main microstructural setting of biotite. In the top pictures, the fanned bioite and elongated biotite are shown. In the bottom picture, the microboudinaged biotite is shown.
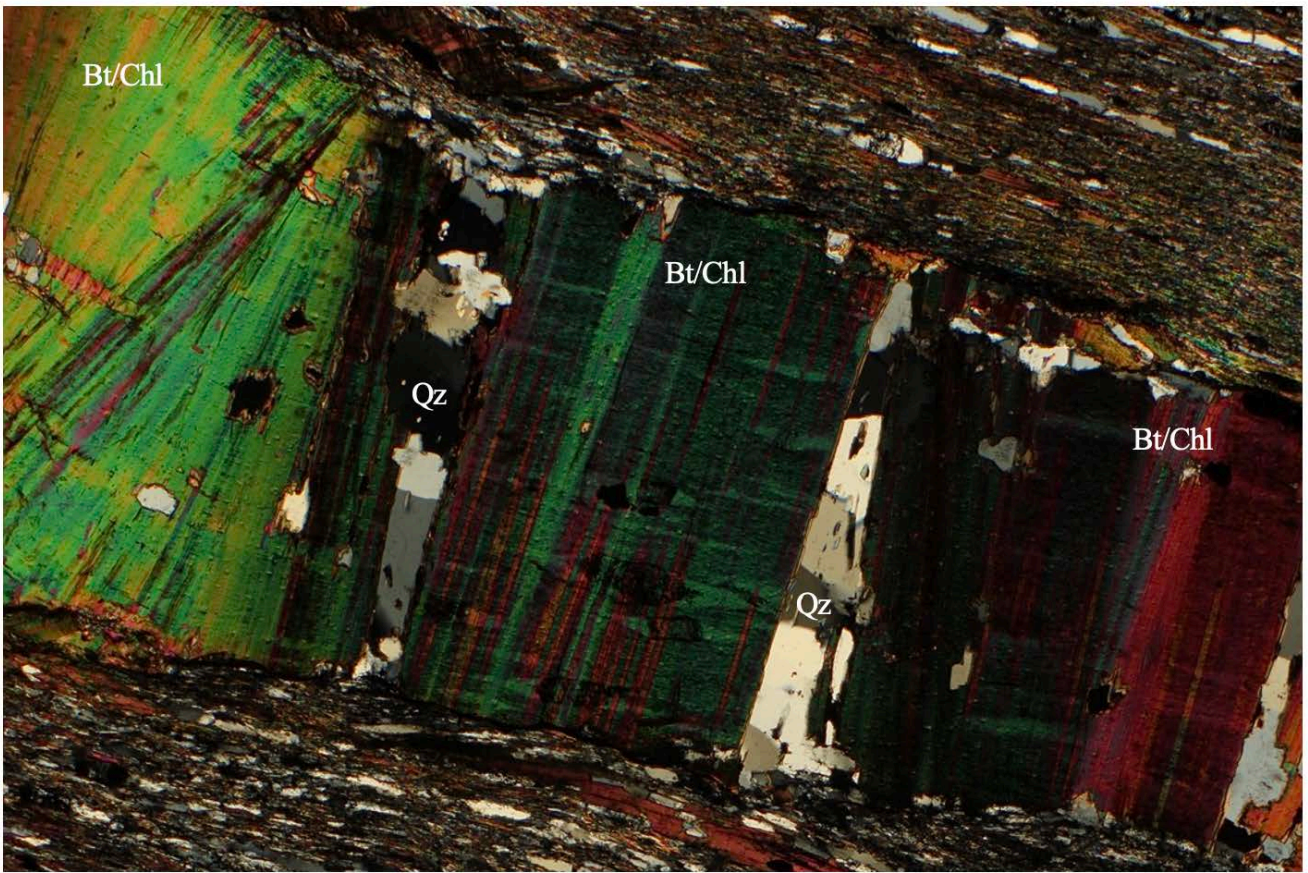
Fig 4.17: microboudinaged biotite with alternating graphite-rich and graphite-free sectors. Coarse quartz (up to 0.7 mm) is found inside some boudins neck. The base of the photo is 2.65 mm long.
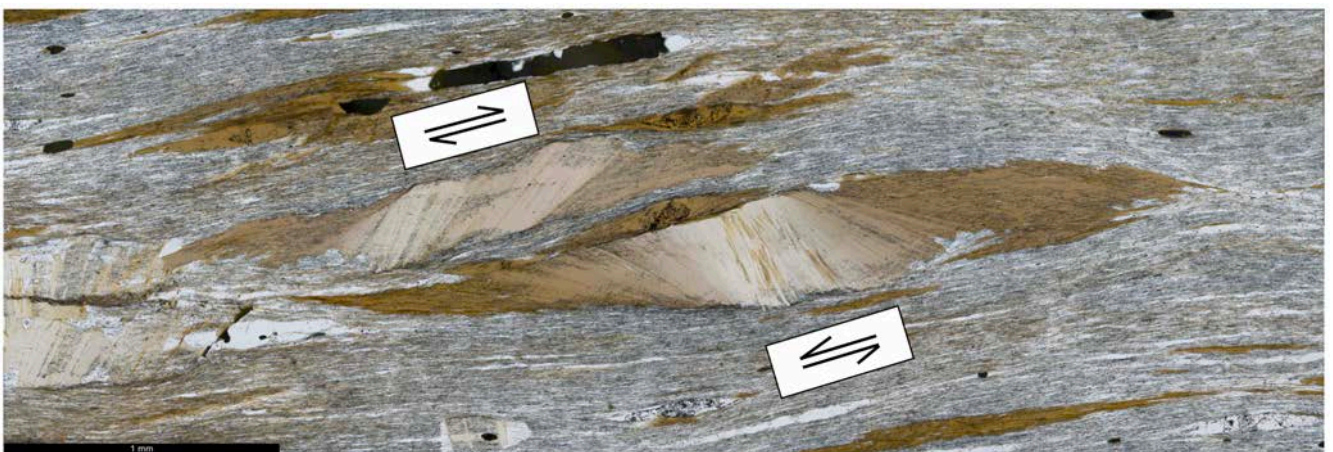

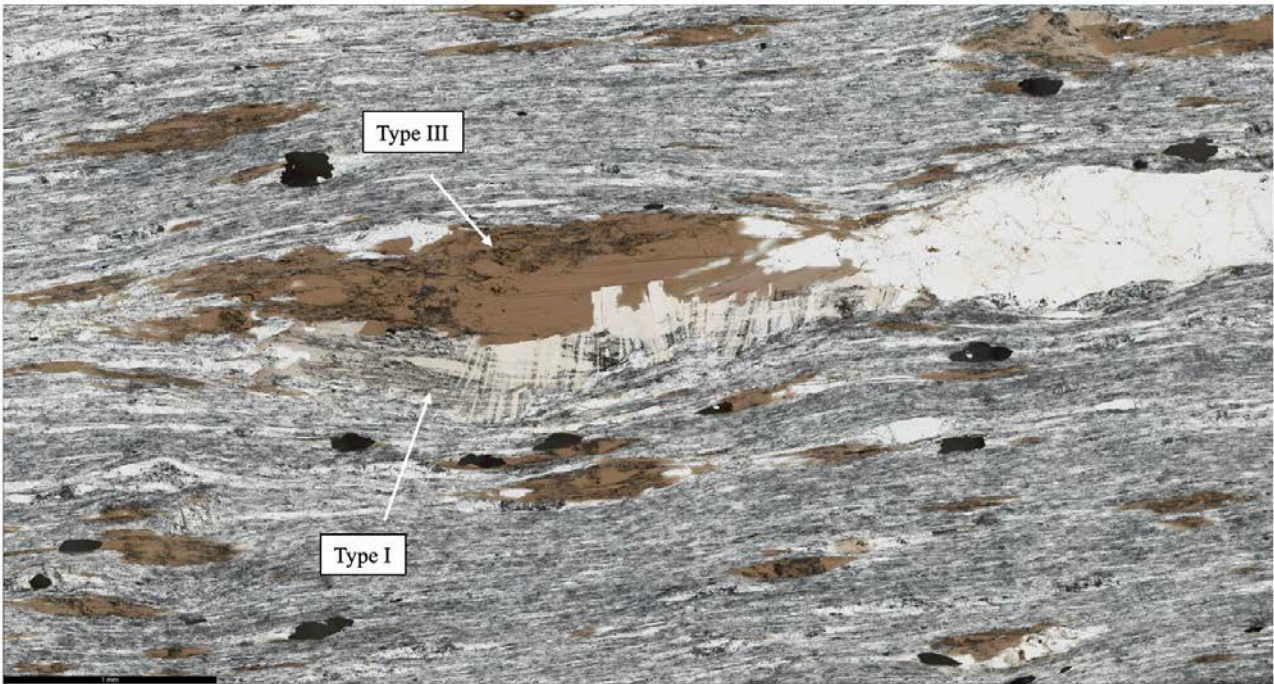Fig. 4.18: dextral and sinistral type II biotites. The black bar is 1 mm long.

Fig 4.19: type III biotite inside a type I biotite. The black bar is 1 mm long.
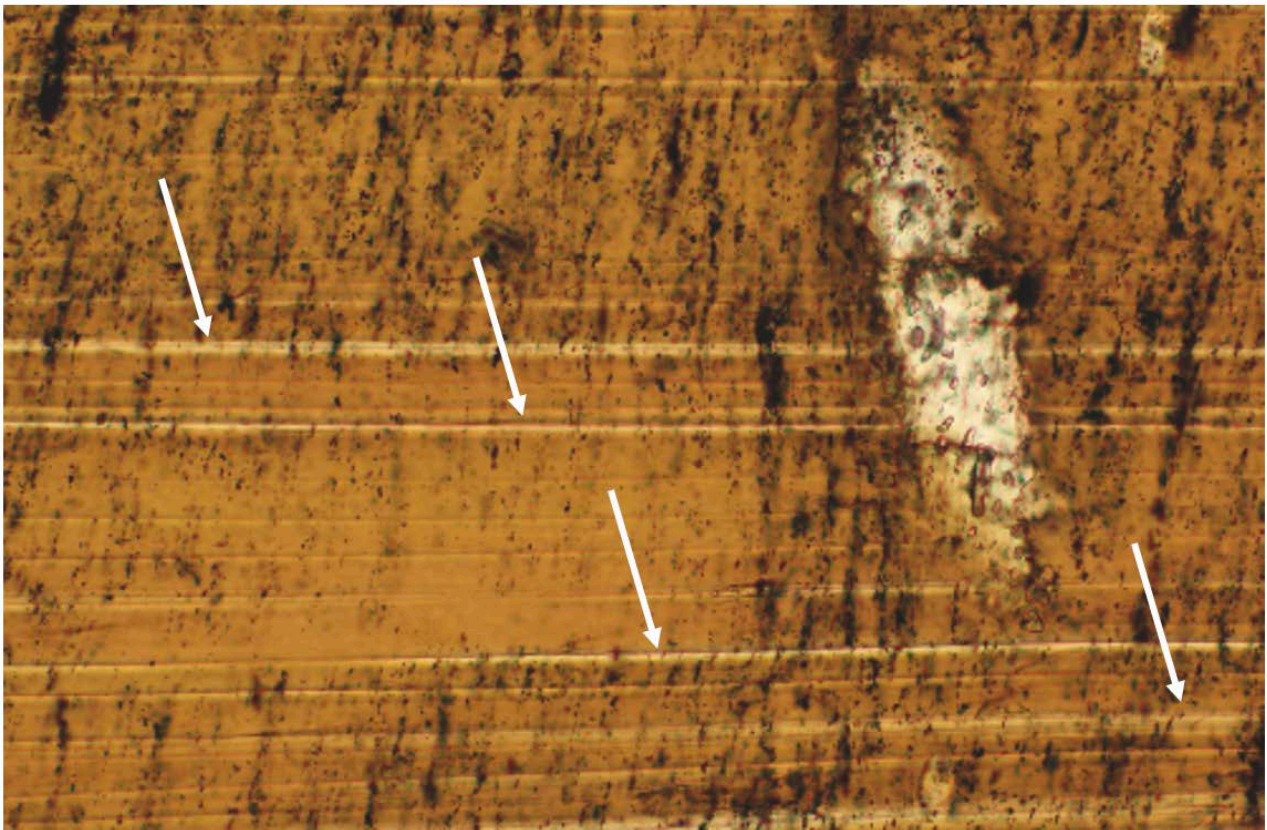

Fig. 4.20: biotite and chlorite intergrowths. Chlorite lamellae are the thin greenish lines inside the larger biotite domains (arrows). The base of the photo is 0.68 mm long.
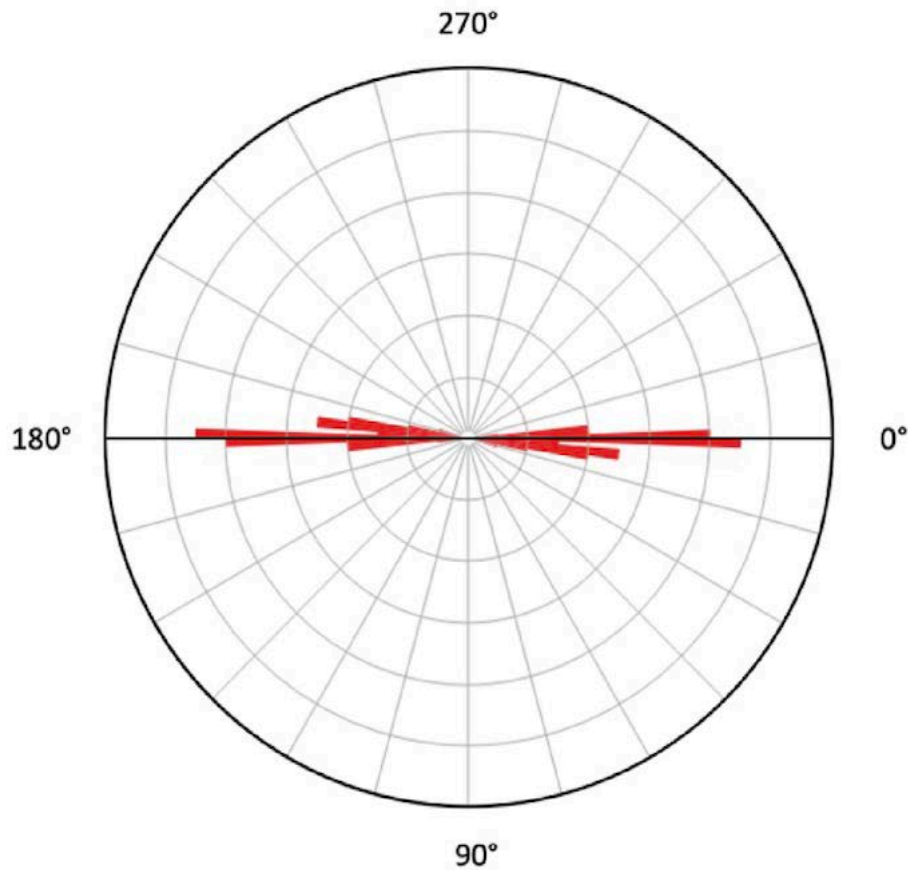
Fig 4.21: rose diagram showing the orientation of biotite porphyroblasts. The foliation of the sample is set at 0°.

4.2.2 Garnet

Garnet displays variable sizes from sample to sample, ranging from 2 mm up to 1 cm (Fig. 4.22). They are often euhedral and show spectacular hourglass distribution of inclusions (Fig. 4.22), and inclusion trails that are continuous with the foliation outside the garnets (4.22). Graphite is the most common inclusion within garnet, that appears very dirty both in the rims and in the cores.
Epidote is also found as an inclusion in garnet from some samples (Fig 4.23)

Fig. 4.22: garnets with hourglass zoning and continuous inclusion trails. The base of the photo is 13.7 mm long.

Fig 4.23: euhedral prismatic and lozenge shaped epidote crystals included in a garnet. The base of the photo is 1.37 mm long.

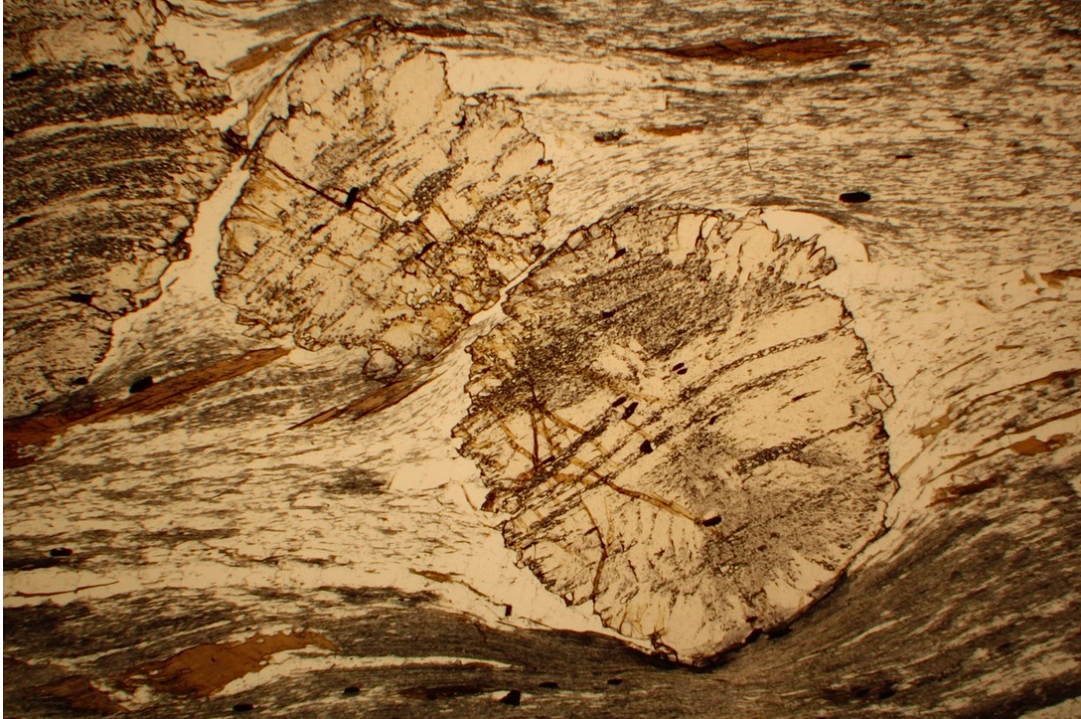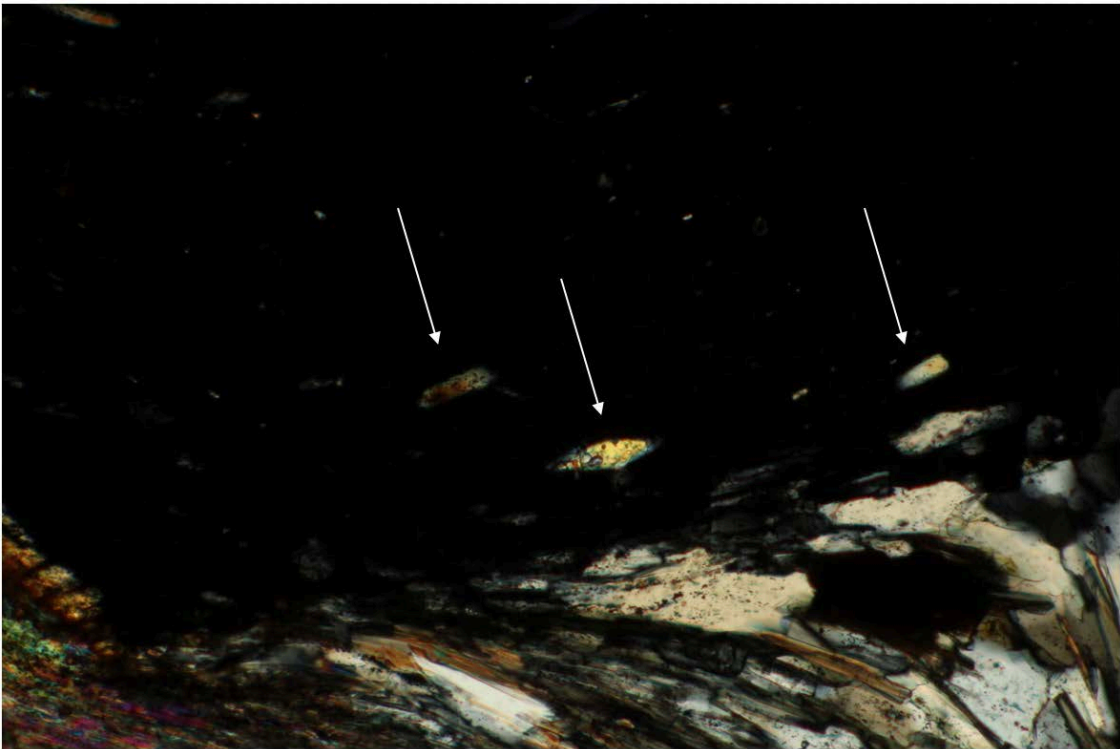Rice et al. (2007), proposed a way to compare predicted the theoretical distribution of inclusions in sector-zoned garnets (Fig 4.24) with the microstructures observed in the natural ones. In the analyzed samples, the inclusions show that graphite forms well-defined type-1 inclusions along the growth pyramids of the crystal, as well as some type-4 fine intergrowth in between the garnet sectors defined by the type-1 inclusions (Fig. 4.22). The distribution of type-1 inclusion and type-4 intergrowths indicate that garnet is mainly rhombododecahedral (four sectors, Fig. 4.25) as confirmed by 3D tomography (see below). Sparse quartz and graphite inclusion are sometimes curvilinear in 2D and may represent a type-2 intergrowth in some garnets (Fig. 4.26).

Graphite, along with the matrix phyllosilicates, also forms well-defined strain caps where garnet abuts the schistosity and is sometimes included in the garnet rims (Fig. 4.27). The deflected foliation outlined by graphite is often included in the most external part of the garnet rims in what seems a post-kinematic static recrystallization (Fig 4.28). Beside the quartz type-2 intergrowth, quartz is also commonly found as inclusion trails in garnet defining the original foliation overgrown by the porphyroblasts (Fig 4.22).

Moreover, these garnets are slightly birefringent with an optical sector zoning, and in fact they have been proved to be of non-cubic symmetry and are instead tetragonal (Cesare et al. 2019).
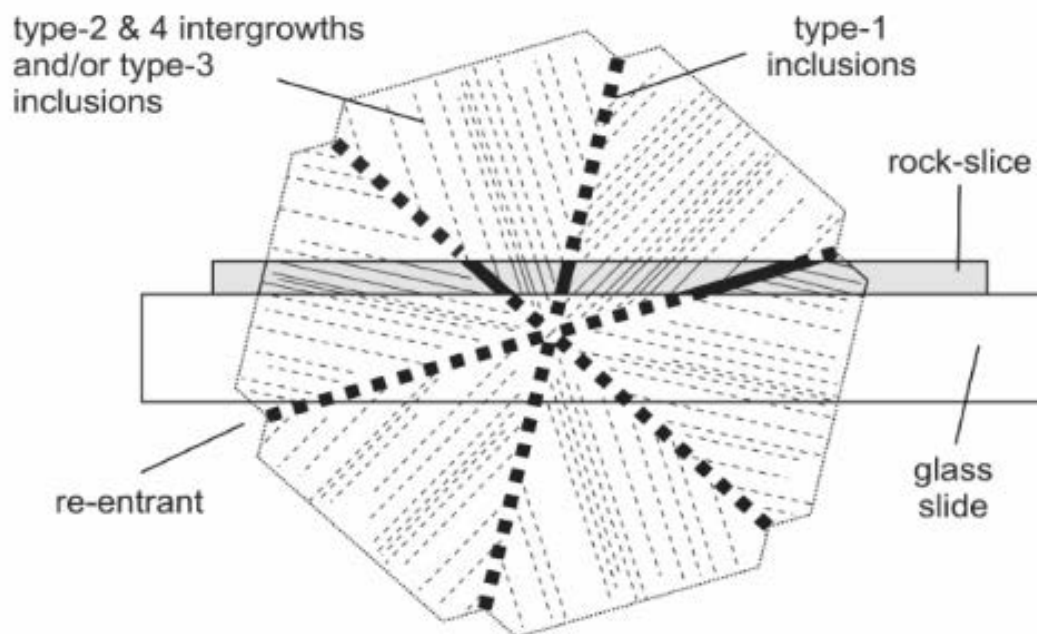
Fig. 4.24: Schematic illustration showing the dependence of type-1 inclusion width and type-2 and 4 intergrowth and type-3 inclusion lengths on section orientation (after Rice et al. 2007).

Fig. 4.25: sector zoned garnet with graphite inclusions. A total of four sectors are visible with two of them being completely inclusion free and two showing type-4 intergrowth. Type-1 inclusions are dividing the four sectors. The base of the photo is 5.3 mm long.
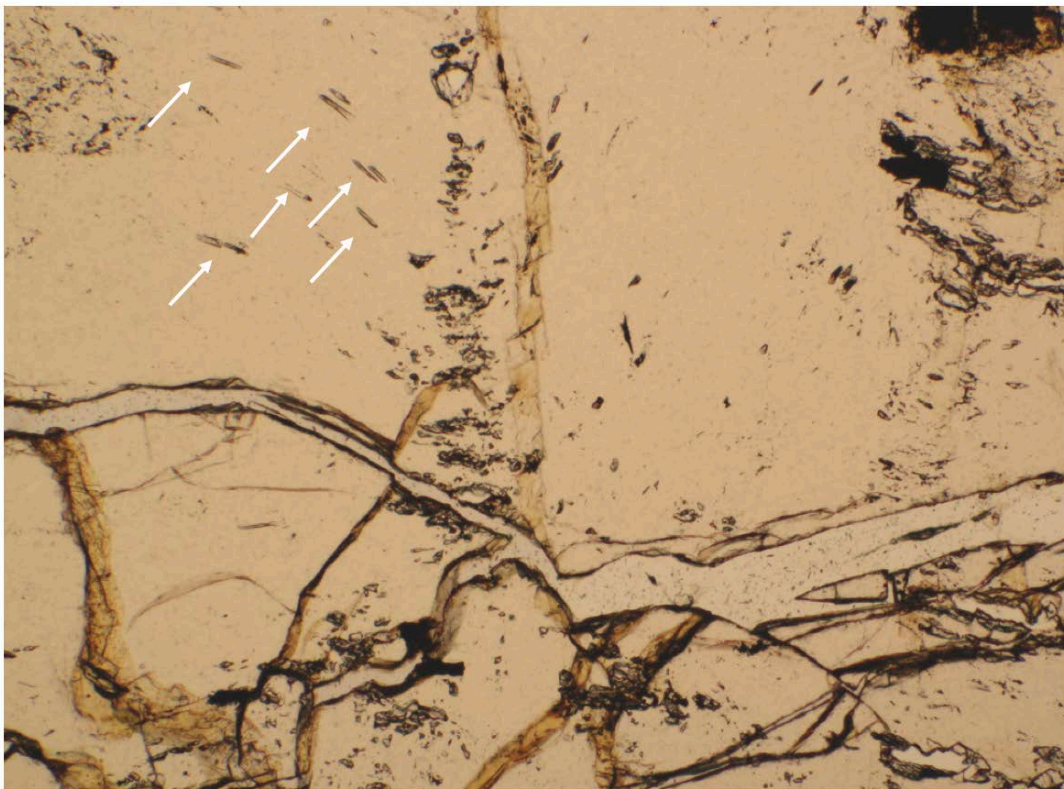
Fig. 4.26: detail of the sparse quartz type-2 intergrowth with their curvilinear shape. The base of the photo is 2.65 mm long.
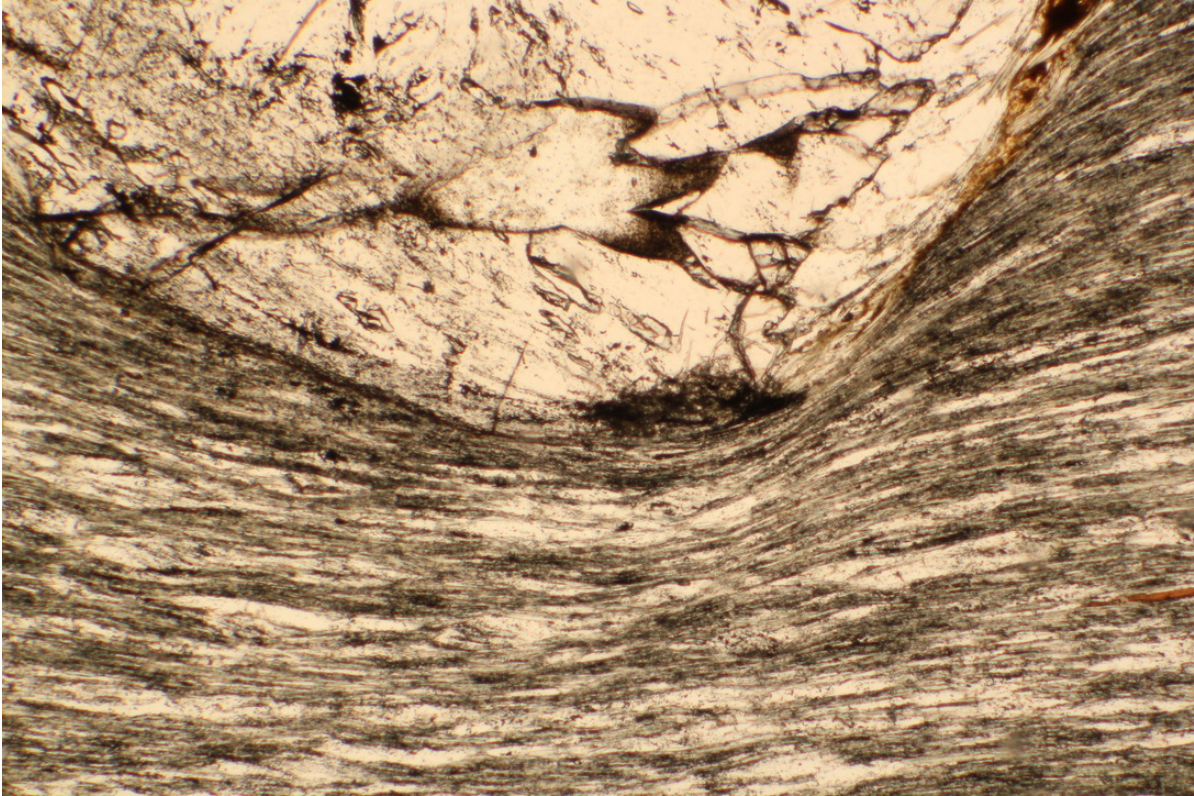
Fig 4.27: strain cap along the edge of a garnet. The base of the photo is 2.65 mm long.
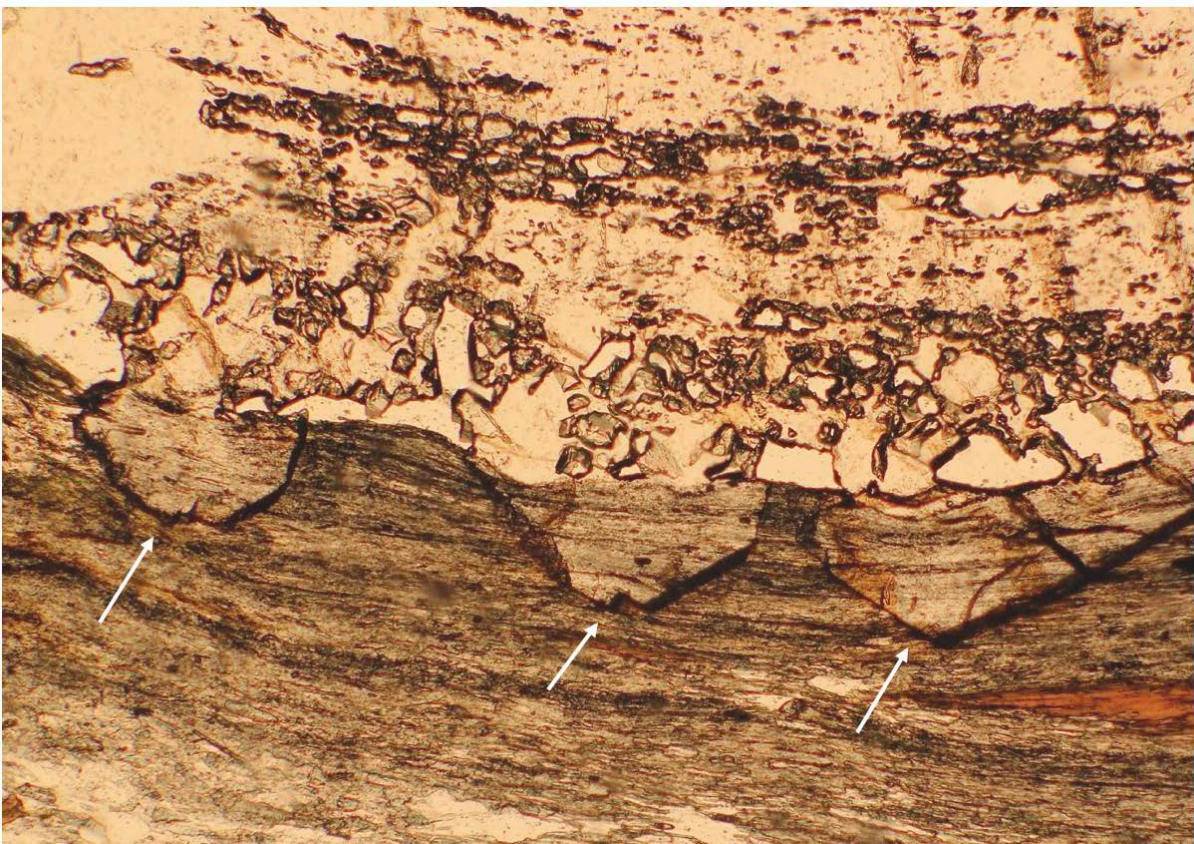
Fig. 4.28: Garnet rim overgrowing the graphite-rich strain cap. The base of the photo is 5.3 mm long.

4.2.3 Ilmenite

Ilmenite porphyroblasts display rectangular sections with sizes ranging from 0.1mm to 1.5mm. They often develop strain shadows that are filled with quartz and with coarse chlorite grains that are clearly in microstructural equilibrium (Fig. 4.29 and 4.30).
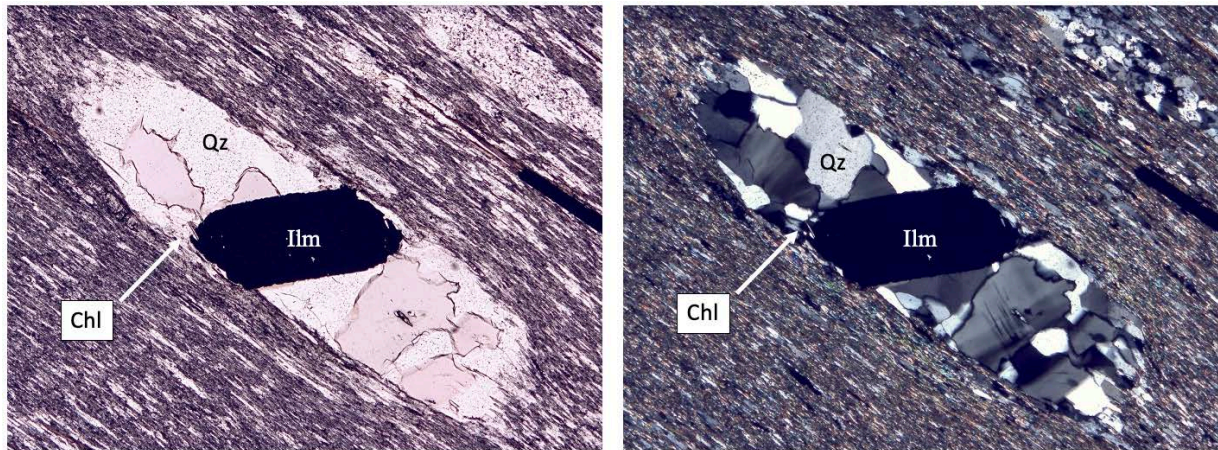
Fig. 4.29: ilmenite crystals with coarse quartz in the pressure shadow. The base of the photo is 2.65 mm long.
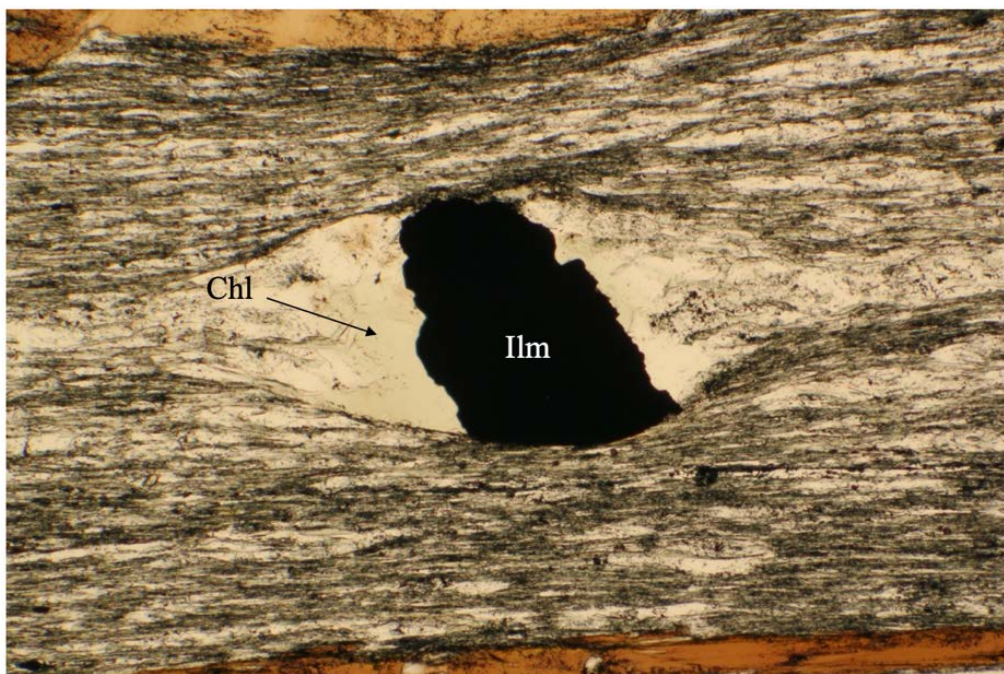
Fig 4.30: ilmenite pressure shadow with chlorite that is microstructurally in equilibrium. The base of the photo is 2.65 mm long

4.2.4 "Ghost crystals"

Microstructures here defined as "Ghosts crystals" have been observed at the thin section scale. These crystals are remnants/pseudomorphs after pre-existing mineral phases that are now completely overgrown and replaced by other minerals. Their original shape is still preserved due to dense accumulations of graphite inclusions. The most common occurrence are ghost crystals replaced by fine quartz and epidote aggregates or overgrown by biotite porphyroblasts (Fig. 4.31). In some cases, microboudinaged ghost crystals are found inside biotites (Fig 4.32). The original mineral is unknown, but they are probably relicts of some carbonates, since 2D sections suggest a rhombohedral shape. In the Passo di Vizze area, minerals such as calcite, dolomite and ankerite have been found and may be the original detrital mineral now transformed into a ghost. A second option could be microfossils. The boudinaged ghost crystals represent a good strain indicator.
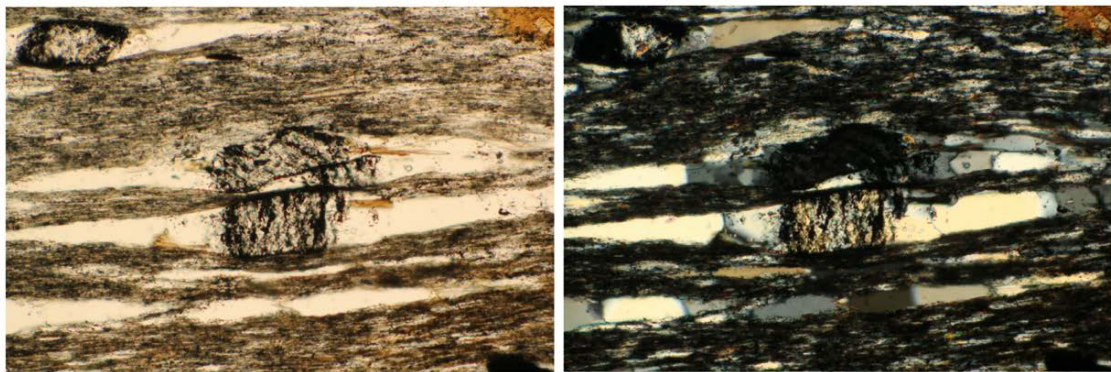
Fig. 4.31: ghost crystals made of fine-grained quartz aggregates. Both the bases of the photos are 1.37 mm long.

Fig 4.32: microboudinaged ghost crystal overgrown by biotite. The base of the photo is 1.37 mm.

4.3 SEM observations

4.3.1 Microstructural observations

Backscattered (BSE) images have provided more information on the very thin intergrowths of biotite and chlorite and on the graphite distribution. Biotite is the heaviest mineral in the image and thus chlorite is darker than it; the darkest minerals are the quartz of the boudins and of the matrix and graphite, with the latter being completely black (Fig. 4.33).
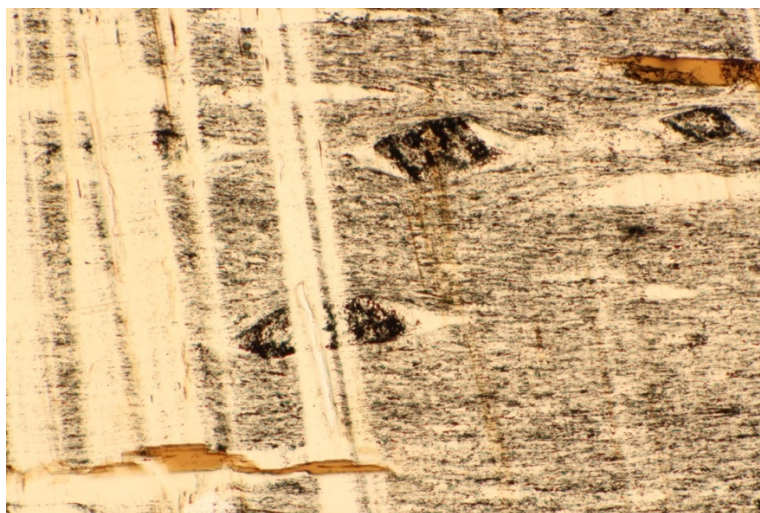
BSE images highlight the intergrowth of alternating chlorite and biotite lamellae that is faintly visible at the thin section scale. Chlorite lamellae are very thin, sometimes even thinner than 1 µm and are only found inside graphite-rich sectors (Fig. 4.33b). BSE images also confirm that no chlorite intergrowths are found in graphite-free sectors (Fig 4.33c).

Some chlorite crystals are found in microstructural equilibrium inside microboudinaged biotite. In this case, chlorite is nearly parallel or at least continuous with the external foliation instead of being perpendicular to it (Fig 4.31d).

4.3.2 Chemical analyses

The compositional characterization of the main minerals is not the main focus of this work, as it will be the main topic of the master's thesis by Simone Bedon. Here, I will be using some of his preliminary data for the microstructural interpretation.

An EDS qualitative analysis has been performed to clearly distinguish biotite and chlorite when investigating the microstructure in order to assess the intergrowths. EDS quantitative analysis have been later performed and, interestingly, biotite composition does not show any major chemical variation between the graphite-rich and graphite-free sectors and the parallel biotites overgrowing the perpendicular ones. In fact, the X_{Mg} of biotite ranges from 0.49 to 0.51, that is a very restricted variation in chemical composition.
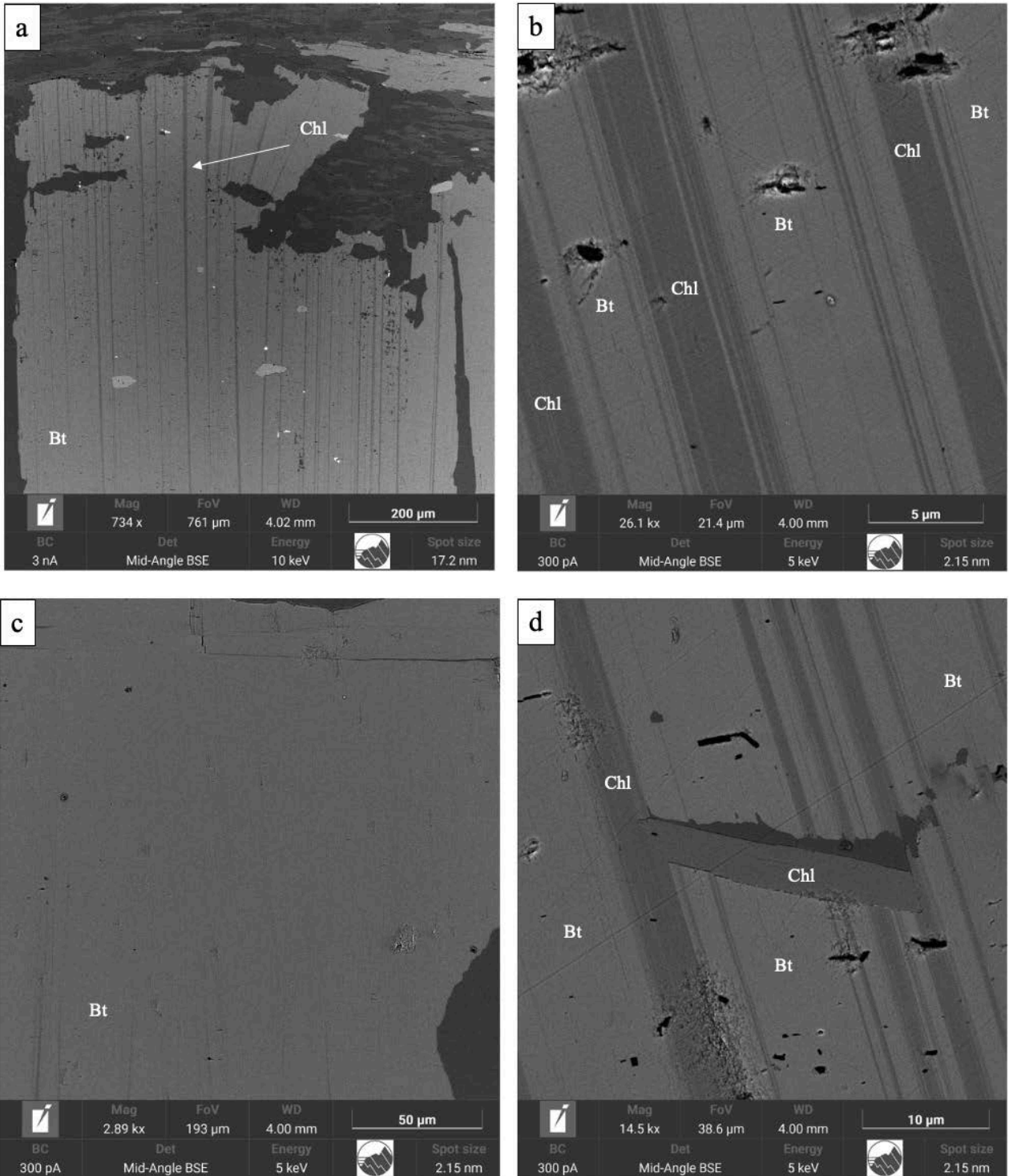
Fig 4.33: SEM BSE images. a: alternating biotite and chlorite lamellae and quartz filling the boudins; b: biotite and chlorite intergrowths. Graphite is present only in these domains; c: graphite-free portion of type I biotite; d: foliation parallel stable chlorite growing within a type I biotite.

4.4 Strain reconstruction

Strain analysis is a useful way to retrieve the state and the amount of deformation the rock has undergone. The strain reconstruction has been performed on microboudinaged biotite porphyroblasts which are well suited for this type of analysis. The strain is calculated using the following formula:

$$Strain\ \% = \frac{Length\ increment}{Initial\ length} \times 100$$

Strain is measured as percentage and is calculated as the ratio between the deformed porphyroblast length variation and its undeformed initial length. In this case, the final length is directly measured on the thin section (Fig. 4.34) and the initial length is calculated as the final length minus the sum of all the length increments. The total length variation is calculated as the sum of all the increments that are basically the boudin necks length – corresponding to the clean, graphite-free portions of porphyroblasts and to the quartz-rich necks - that are also measured on the thin section (Fig. 4.35). Strain calculations have been performed on 13 crystals with boudin necks composed of both biotite and quartz together and biotite only. Tab 4.1 summarizes the data and strain calculations, while also providing other values such as the total increment and the biotite and quartz increments for all the measured porphyroblasts, as well as the quartz/biotite increment ratio.

Fig. 4.34: length measurement on crystal VIZ01-6P (9).
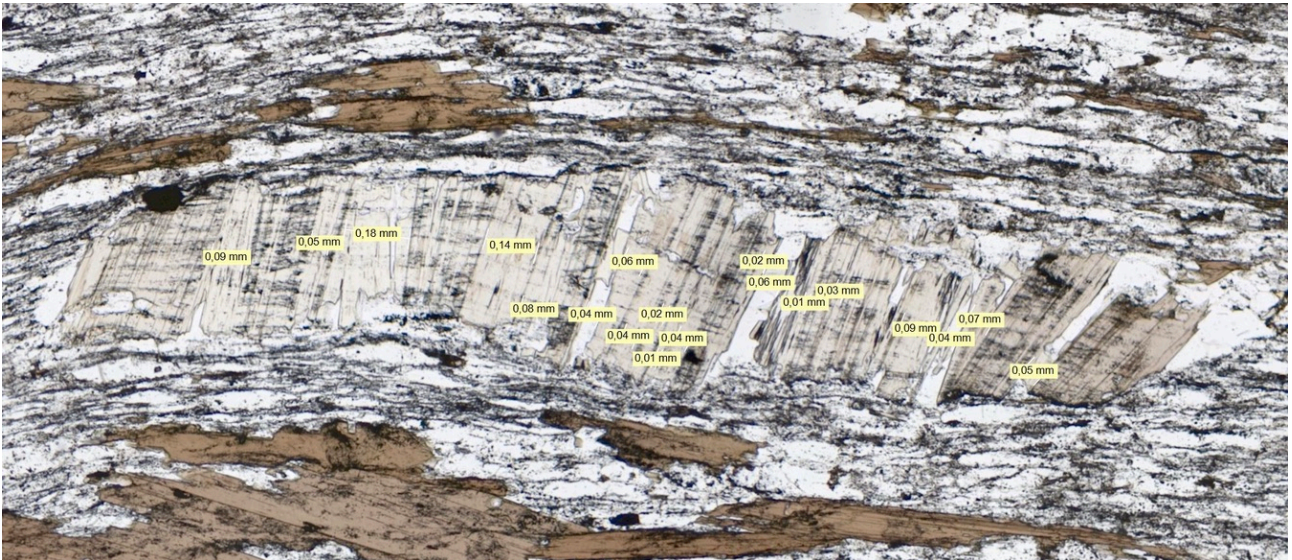
Fig. 4.35: boudin length measurements on crystals VIZ01-6P (9).

	Initial length (mm)	Final lenght (mm)	Total Strain (%)	Bt + Qz increments (mm)	Bt increments (mm)	Qz increments (mm)	Qz/Bt ratio
VIZ01-6P(1)	2.3	2.5	12	0.3	0.3	0.0	0.00
VIZ01-6P(2)	3.9	8.5	117	4.6	3.6	1.0	0.29
VIZ01-6P(3)	3.3	6.0	81	2.7	2.5	0.2	0.07
VIZ01-6P(4)	3.8	7.0	82	3.1	2.9	0.3	0.10
VIZ01-6P(5)	3.5	6.3	77	2.7	2.6	0.1	0.06
VIZ01-6P(6)	4.7	8.9	88	4.2	4.0	0.2	0.05
VIZ01-6P(9)	1.9	3.0	59	1.1	1.0	0.1	0.14
VIZ01-6P(10)	3.6	5.4	52	1.9	1.9	0.0	0.00
VIZ03-3P (1)	3.8	5.4	43	1.6	1.5	0.2	0.12
VIZ03-3P (2)	1.5	2.5	65	1.0	1.0	0.0	0.00
VIZ03-3P (3)	1.4	2.9	115	1.6	1.3	0.3	0.21
VIZ03-3P (4)	2.6	5.0	92	2.4	2.1	0.3	0.13
VIZ03-3P (5)	1.7	3.9	131	2.2	1.7	0.4	0.26
VIZ03-3P (6)	3.3	5.0	53	1.7	1.3	0.4	0.28
Average	3.0	5.4	81	2.4	2.1	0.3	0.13

Tab 4.1: summary of the strain calculations. The highlighted samples -VIZ01-6P (1), VIZ01-6P(10) and VIZ03-3P (3)- are sample with boudins made of biotite only.

The total strain of the porphyroblasts is plotted on an initial length against final length plot (Fig. 4.36). The lines are representing the strain percentage where the 100% line represent the undeformed state. The majority of the values are found in between the 50% and the 100% strain with a mean strain of 76%. This means that on average, biotites final length is less than double the initial one.

Fig. 4.36: Total strain plot.

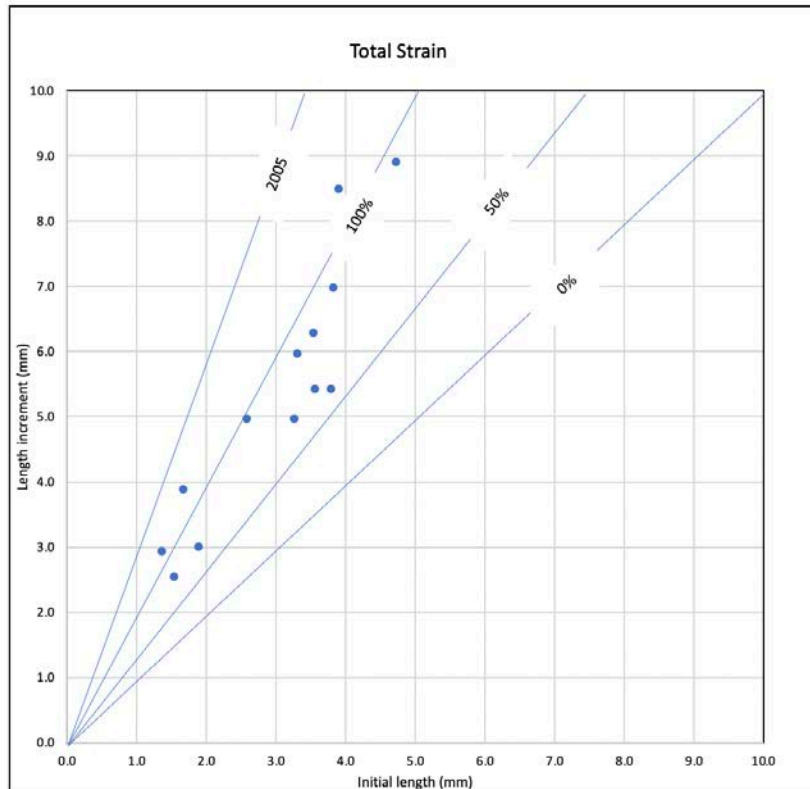The quartz/biotite ratio is plotted against the total strain (Fig. 4.37) and the values are seemingly correlated in a positive way, that indicates how higher quartz/biotite ratios are usually correlated with higher strain values.
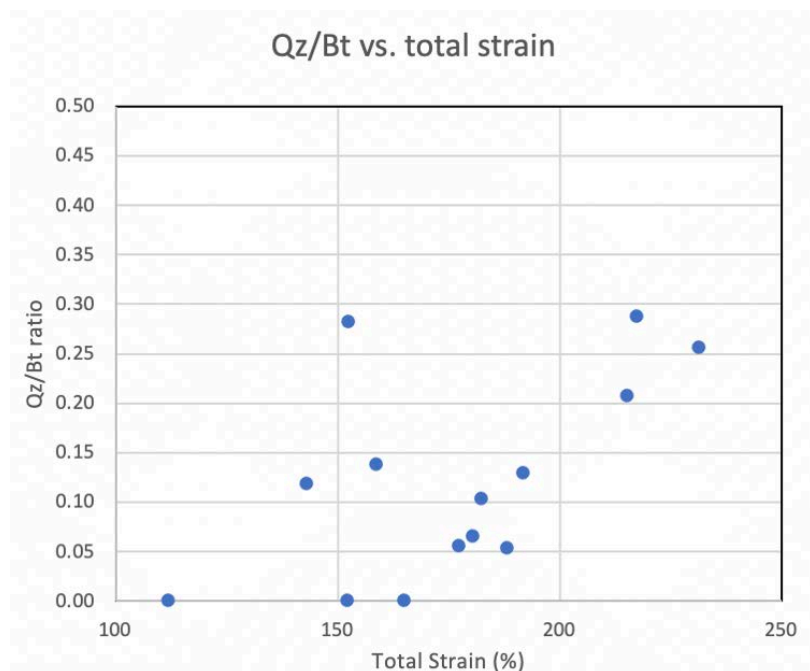

Fig. 4.37: quartz/biotite ratio against total strain plot.

Along with the porphyroblast long axis, the short axis was measured, too. With these two measures it is possible to calculate the aspect ratio of the minerals and to compare it to the crystal orientation with respect to the foliation. The measures have been divided among the three main types of biotites with the aim of looking for a minimal length at which biotite could have rotated. Unfortunately, there are no correlation between the two as seen in Fig. 4.38. The plot is also showing that biotites are well aligned with the foliation and so they reached the strain required to become parallel with the foliation at lower strain that currently measured

Fig 4.38: Orientations of biotite porphyroblasts (y axis) against aspect ratio (x axis) plot for the three different biotite types. Type I biotites (orange), type II (blue) and type III (green) biotites doesn't show any correlation between the two considered values

4.5 3D microstructural analysis

The 2D information from the several thin sections analyzed have been complemented with 3D data from microtomography. Sayab et al. (2015), states that the spatial distribution, shape and orientation must be inferred from the combination of several 2D sections and is, in fact, an intrinsic problem in the study of microstructures. With μCT, from a fairly small hand sample of centimetric scale, it is possible to perform a fabric analysis by retrieving the location, size, shape, orientation and contact relationships with other objects (Ketcham et al. 2004).

For this study, the aforementioned approach is very useful and interesting as it permits to explore the 3D geometry of samples up to the hand sample scale to define the distribution of minerals inside a

sample in a non-destructive way and then to extract data such as the spatial orientation and shape of the porphyroblasts. The microtomographic approach has been applied to one representative sample of the Furtschaglschiefer unit for a 3D reconstruction of microstructures related to the main porphyroblasts (biotite, garnet, ilmenite).

Images acquired from μCT scans are grey-scale images based on the elemental composition of the minerals.

Mineral segmentation and separation, and as such image analysis in general, is subjective and sometimes may be biased.

In order to obtain the final separated images, the grey scale image is denoised, then segmented and finally separated. The final product is a binary image containing only the selected separated mineral. Figure 4.39 shows all the steps from the original image to the separated one. Starting from the original image (Fig. 4.39a), denoising was computed using a median filter (Fig. 4.39b), and the segmentation of the image was computed using a watershed algorithm in order to discriminate the phases in the image (Fig. 4.39c), the image is then thresholded to choose the phase to be separated. After the separation (Fig. 4.39d), the binary image is post-processed by means of different plugins such as erosion, dilation, opening, closing, remove small spots (Fig 4.39e and 4.39f) in order to remove artifacts or unwanted particles. Finally, the image is labeled (e.g., each particle is assigned an identity and a lavel), and it is possible to compute the shape analysis that can be further filtered in order to extract only some of the data or to further remove artifacts.
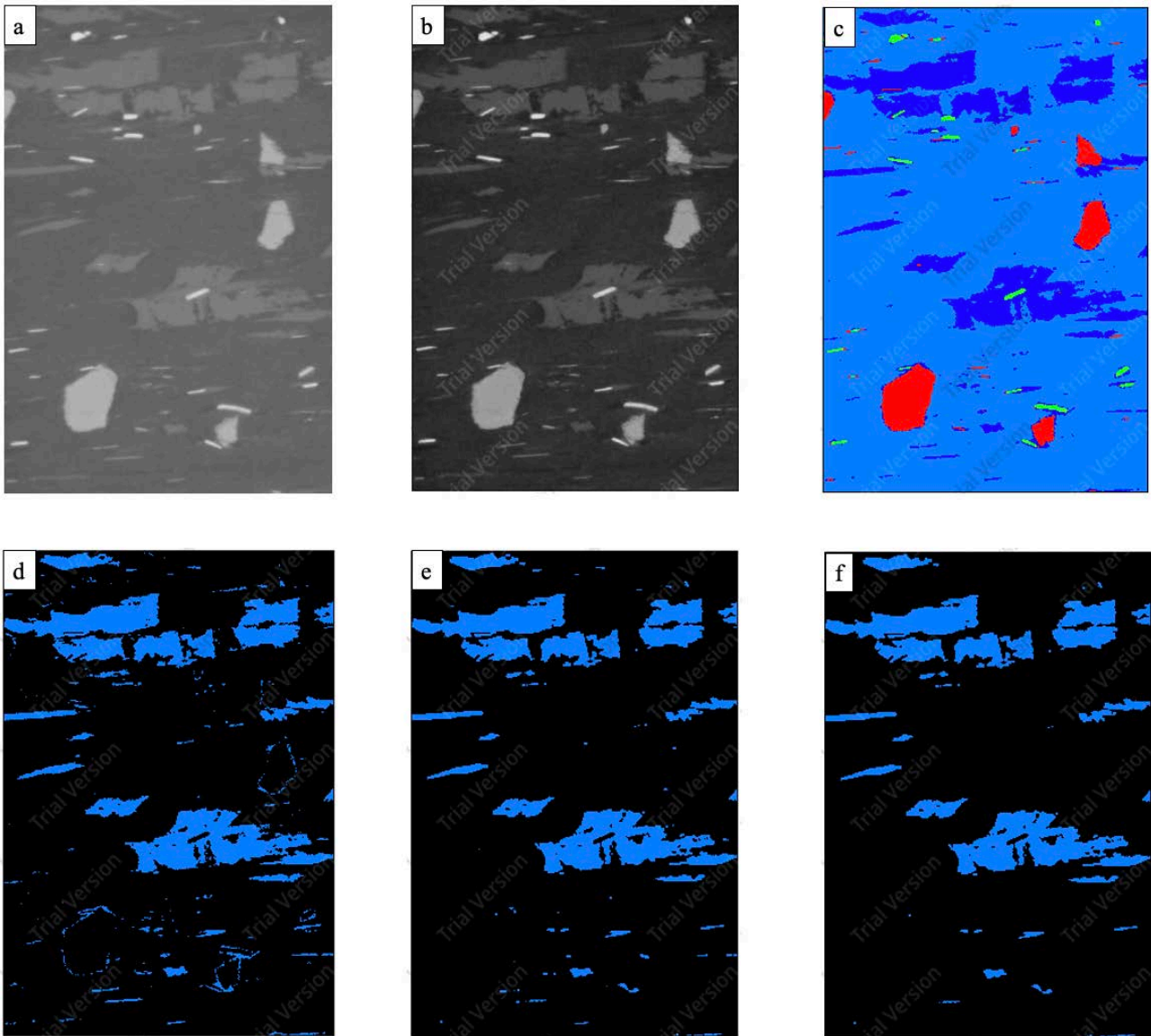
Fig 4.39: step by step separation of biotite. a: original micro-XCT slice; b: filtered image; c: segmented image showcasing the different basins computed by the watershed algorithm; d: separated biotite; e: post-processing with the "opening" plugin to remove the garnet outlines from Fig. 4.37d; f: final post-processing with the "remove small spots" plugin to remove the small artifacts in the matrix.

Using the final cleaned and separated images, it is possible to generate 3D renders for each mineral in order to better visualize the mineral distribution. As an example, Fig 4.40 shows the distribution of the main porphyroblasts that have been studied at the thin section scale. The single minerals description and the strain analysis performed on them is explained in the following sections.

2000 µm
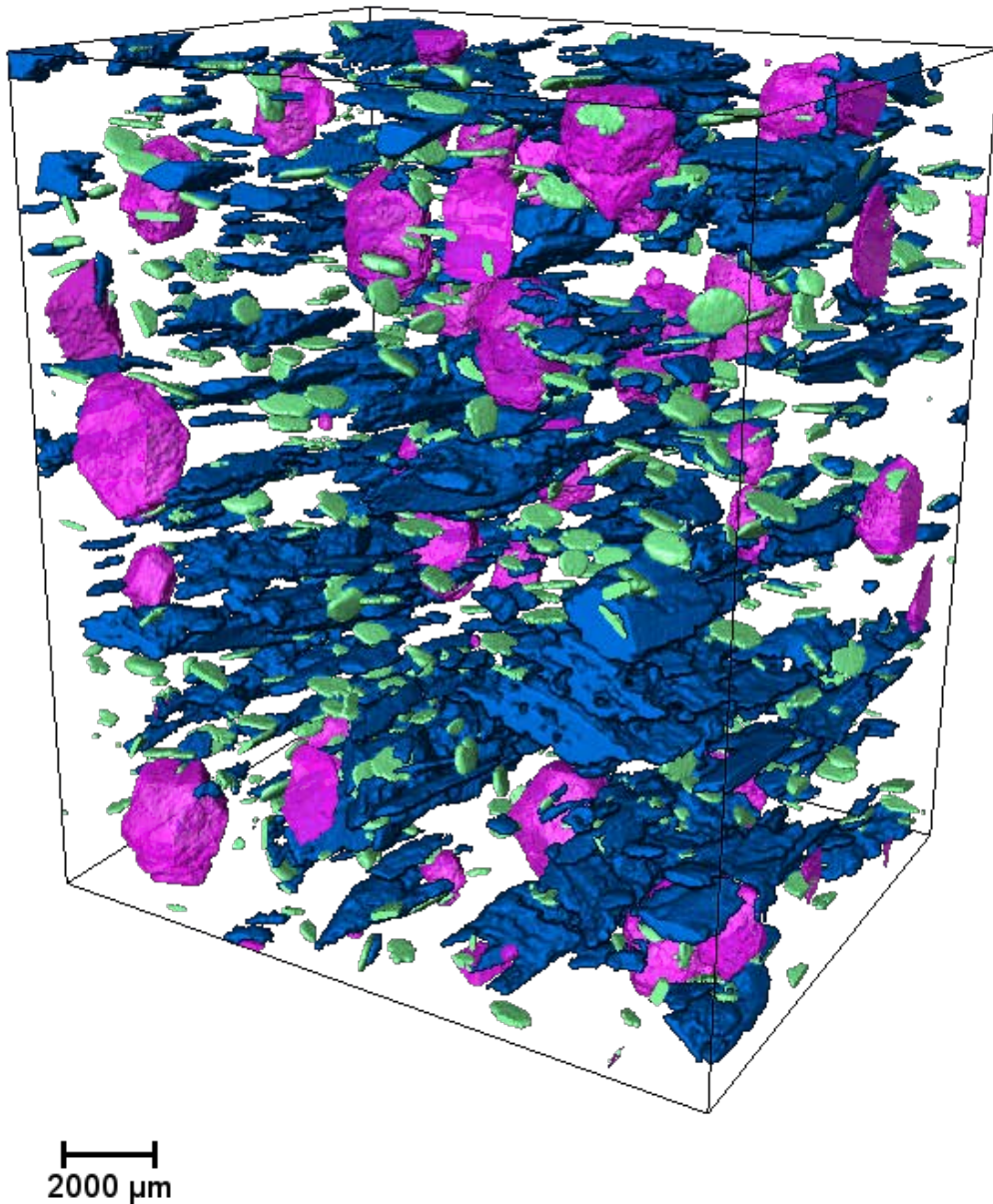
Fig. 4.40: complete 3D render of biotite (blue), garnet (pink) and ilmenite (green) porphyroblasts in the investigated sample.

4.5.1 Biotite

The 3D reconstruction of biotite is showing the foliation that is highlighted by the larger crystals and the alignment of the single porphyroblasts that define the strong lineation is evident. Fig 4.41 and Fig. 4.42 show the distribution and the shape of biotite and are, respectively, the total biotite volume and a filtered volume with a threshold at 9.7×10^9 µm^3. A shape analysis has been performed on the filtered volume and using the eigenvalues of the long, intermediate and short axis of biotite crystals, the ratio between long and intermediate axis (here defined as "a") and intermediate and short axis

(here defined as "b") have been calculated and then plotted, in order to create a Flinn diagram to define the type of strain the biotites underwent (Fig. 4.43). The shape of the strain ellipsoid can be estimated by calculating with the following formula:

$$K = \frac{(a-1)}{(b-1)}$$

The value of K indicates the shape of the ellipsoid and the type of strain. For values higher than 1 the strain is prolate (constriction), for values equal to 1 the strain is plane (no deformation) and for values lower than 1 the strain is oblate (flattening). For biotite, the mean K value is 3.3, indicating prolate strain.

It has also been possible to calculate the orientation of biotite long axes from the eigenvector values. A shape analysis was then carried out by plotting the orientation of biotite long axes on a stereographic projection (Fig. 4.44). In Fig. 4.44, the lineation of the rock is defined by the NS equatorial plane and is highlighted by a black line. Biotite long axes are showing concentrations along a NS direction (North is arbitrary) and it is possible to say that biotite elongation axes are parallel to the lineation.

2000 μm
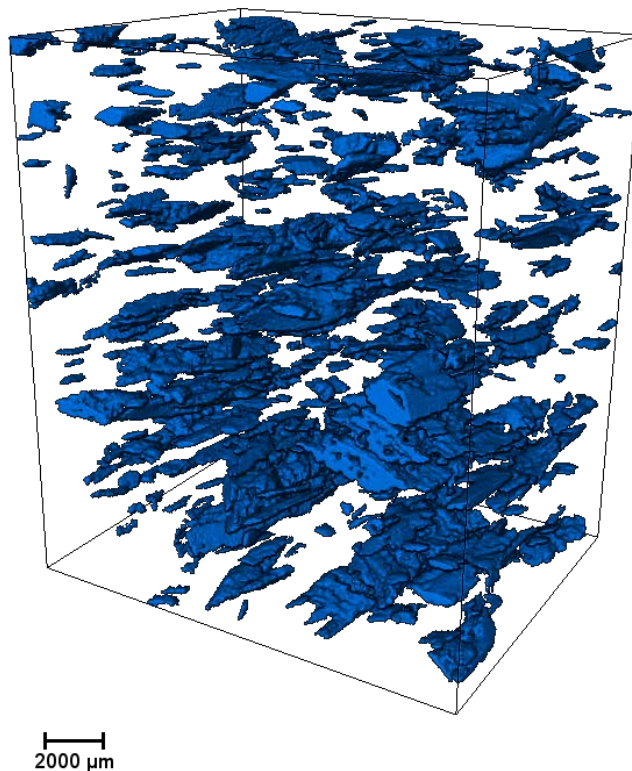
Fig. 4.41: 3D render of the total biotite volume.
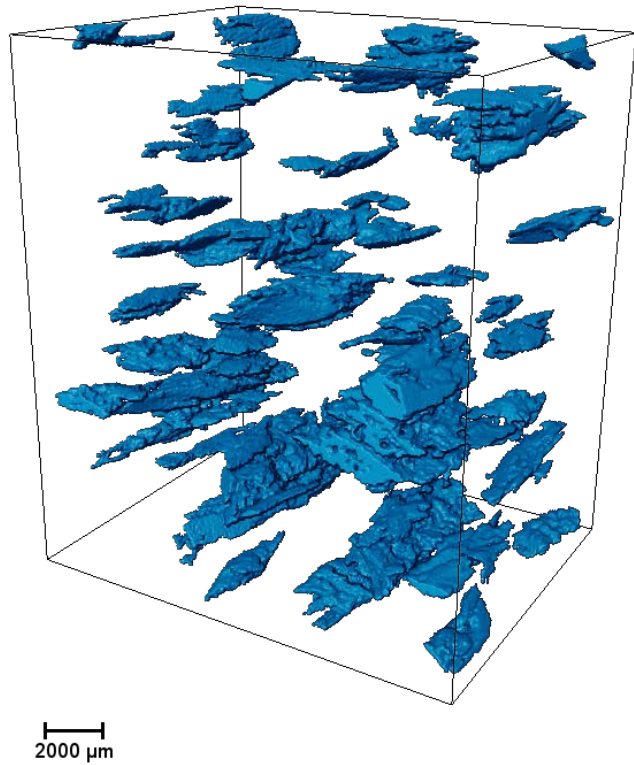
Fig. 4.42: 3D render of the filtered biotite volume.
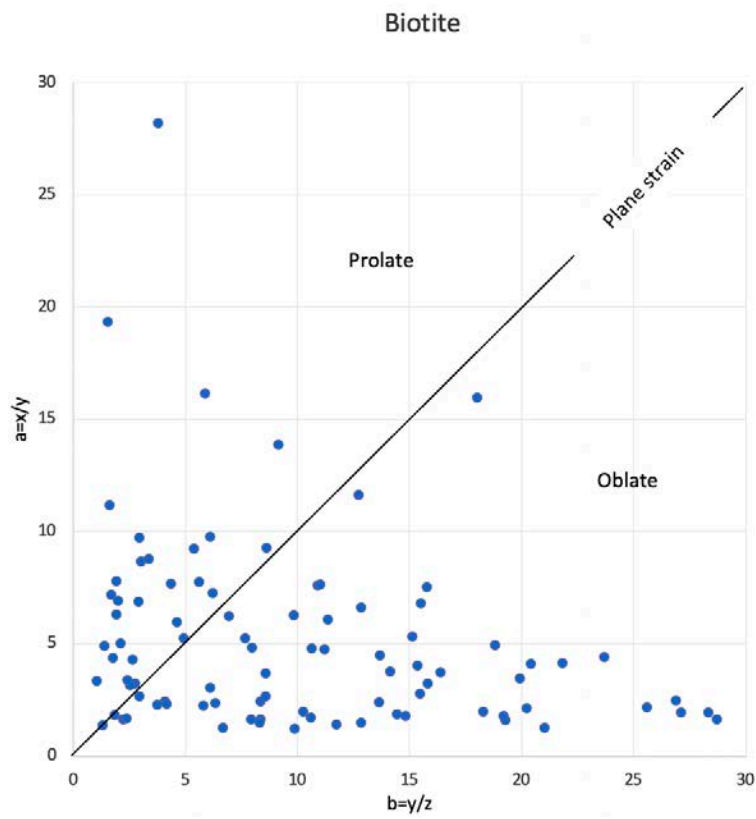
Fig. 4.43: biotite Flinn diagram. The plotted data are the 100 biggest biotites filtered by volume.

Fig. 4.44: Lower hemisphere stereonet projection of biotite long axes. Biotite lineation is highlighted by the NS black line. Biotite long axes are parallel to the lineation.

4.5.2 Garnet

The 3D rendering (Fig. 4.45) shows the evident euhedral shape of the porphyroblasts and confirms the hypothesis of rhombododecahedral garnets (Fig 4.45, Fig 4.46, Fig 4.47) as suggested by the sector zoning of the graphite and quartz inclusions. The 3D rendering shows that some very small garnets (smaller than 200 μm) are present but were not observed during the petrographic analysis. Garnet has been filtered with a threshold of 6.2×10^9 μm^3 in order to isolate only the largest garnets (Fig 4.46).
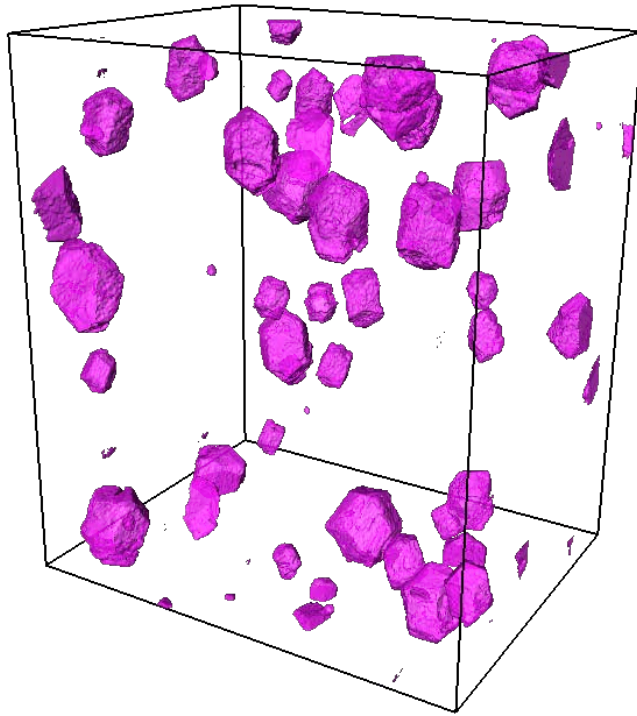
2000 μm

Fig 4.45: 3D render of the total garnet volume.
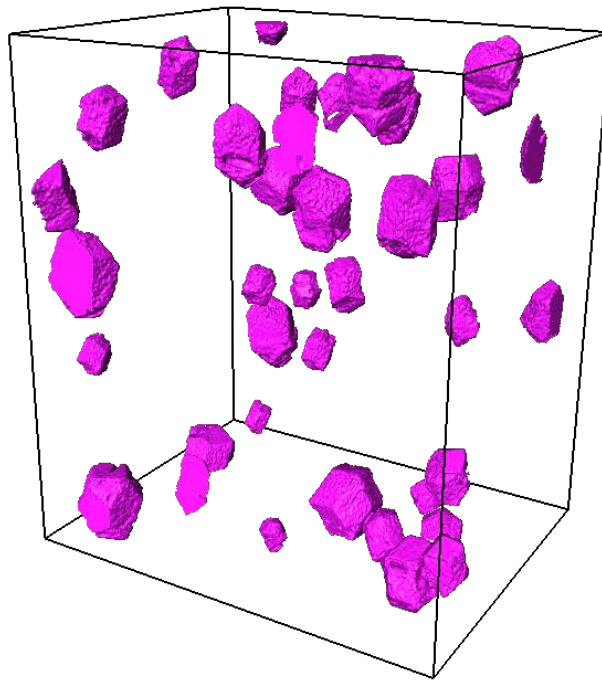
2000 μm

Fig. 4.46: 3D render of the filtered garnet volume.

Fig. 4.47: two views of a 3D render of a euhedral rhombododecahedral garnet. The facets are clearly distinguishable, hence the definition of the symmetry.

4.5.3 Ilmenite

The 3D reconstruction shows that nearly all the ilmenite crystals are flat and are almost coin-shaped with a faint elongation along the major axis (Fig 4.47) and the rectangular section visible at the thin section scale are cut effects arising from such shape. As before, ilmenite volume has been filtered at 1.2×10^8 μm³ threshold in order to remove some artifacts (Fig. 4.48).

A shape analysis on ilmenite porphyroblasts has been carried out by plotting the orientations of long and intermediate axis of the crystals by calculating the orientation from the eigenvectors values. Several ilmenite crystals are iso-oriented parallel to biotite lineation as seen on the ilmenite long axis

stereographic projection, meaning that that ilmenite porphyroblasts are parallel to the foliation (Fig. 4.49). Instead, intermediate axes are all perpendicular to biotite lineation and foliation (Fig. 4.50). The scattering of the point in Fig. 4.49 and 4.50 are caused by the similar values of the long and intermediate axes values that are very similar given the nearly circular shape of the crystals.
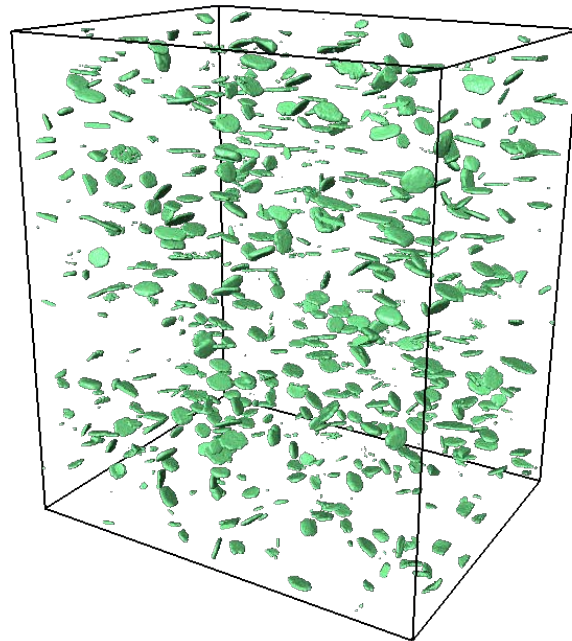
2000 µm

Fig. 4.47: 3D render of the total ilmenite volume.
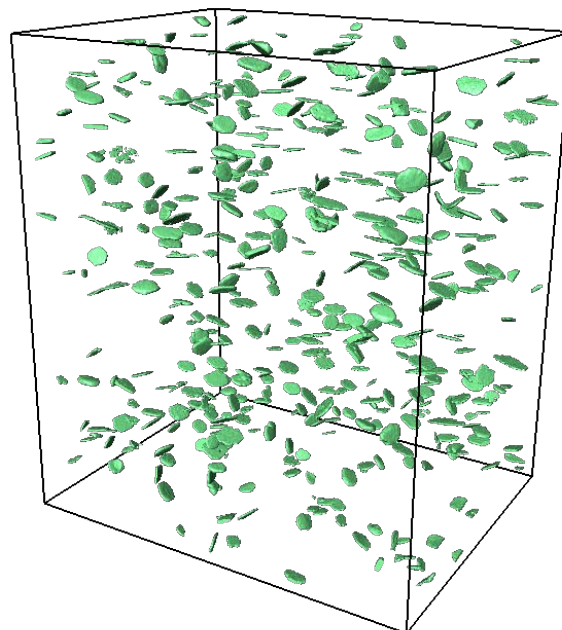
2000 µm

Fig. 4.48: 3D render of the filtered garnet volume.
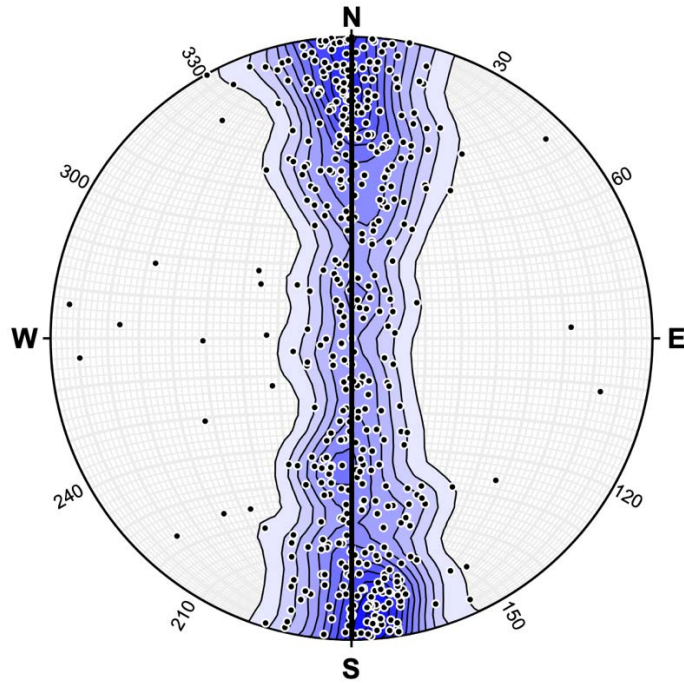
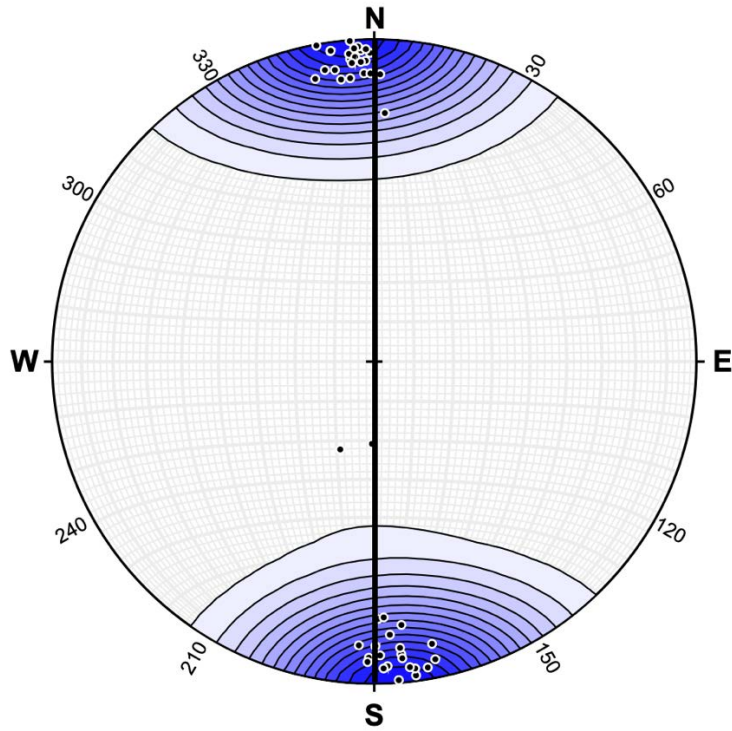Fig 4.49: Lower hemisphere stereonet projection of biotite long axes. Foliation is highlighted by the NS black line. Ilmenite long axes are parallel to the foliation.
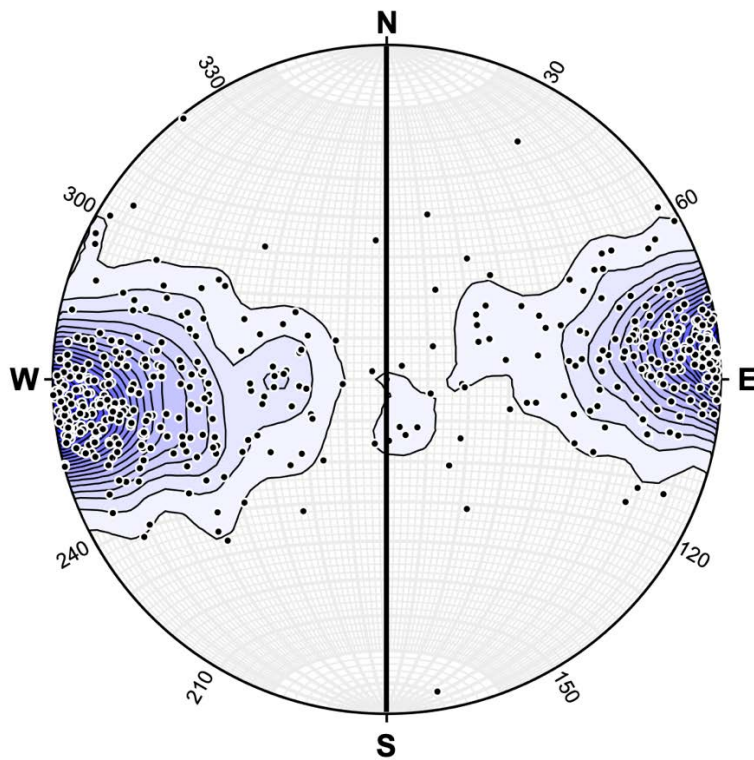

Fig 4.49: Lower hemisphere stereonet projection of biotite long axes. Foliation is highlighted by the NS black line. Ilmenite intermediate axes are perpendicular to the foliation.

5 Discussion

5.1 Results summary

The studied samples display a mineral paragenesis that attests for metamorphic conditions transitional between the upper greenschist facies and the lower amphibolite facies. This is supported in particular by the presence of stable chlorite both in the matrix and inside ilmenite pressure shadow, and by the growth of staurolite in a few samples.

Biotite is typically found in three main microstructural settings (Fig. 4.16) that have been defined by the cleavage (that coincides with the (001) plane of biotite) orientation with respect to the main foliation of the schists: type I (microboudinaged, perpendicular cleavage), type II (fanned, oblique cleavage) and type III (elongated, parallel cleavage). The microboudinaged type I biotite porphyroblasts show graphite-rich and graphite-free sectors with necks made of biotite and quartz (Fig. 4.16). Strain calculations on type I biotites show an average increase in length of 76% (from 12% to 131%). Also, the quartz/biotite ratio increases with the total strain value (Fig. 4.37). Aspect ratio and orientation analysis among all types of biotites did not reveal any possible minimal rotation length, in fact all biotites share the same orientation with respect to the matrix with a variability of ±10° (Fig 4.21 and 4.38).

An almost complete lack of oblique fabrics, beside some locally deformed foliation inside type II biotite, has been observed throughout the samples. The aforementioned type II biotites are fanned and show both dextral and sinistral shear sense, without a prevailing direction (Fig. 4.18).

Graphite-rich sectors are characterized by the intergrowth of alternating biotite and chlorite parallel lamellae, while graphite-free sectors are only composed of biotite (Fig 4.17, Fig. 4.33b and c). The optical observation is confirmed by BSE SEM analysis showing that chlorite lamellae can be <1μm in thickness (Fig. 4.33b). Biotite compositions in graphite-rich and graphite-free sectors are similar and show limited variation of X_{Mg} within ±1%.

μCT helped characterize the 3D distribution, size and shape of elongated biotite porphyroblasts of all types (Fig. 4.41). The lineation of the sample is evident also by the 3D analysis. The shape analysis results, plotted on a Flinn diagram (Fig. 4.43), reveals an oblate strain while the mean K value indicates prolate strain. This contrast is probably caused by the fact that the Flinn diagram for strain type assumes a spherical starting shape for the crystals, but since biotite is elongated to begin with, it does not apply perfectly to these porphyroblasts. Also, the K value is a mean of all the K values of

each porphyroblasts meaning that large biotite can shift the mean value towards more prolate strain even though many data points fall into the oblate strain domain.

Garnets are often euhedral and show both continuous inclusion trails (Fig 4.22) and hourglass sector zoning (Fig. 4.25) depending on the type of matrix they overgrew. Inclusions are mainly composed of graphite, quartz and rare epidote (Fig. 4.22, Fig. 4.23 and Fig 4.25). Graphite usually is included from the strain caps that are in places overgrown by further post-kinematic garnet rims (Fig. 4.28). Graphite also defines type-1 and type-4 inclusions (Fig. 4.25) according to the typology defined by Rice et al. (2007) (Fig. 4.24). Quartz defines rare type-2 intergrowth (Fig 4.26). From the 2D distribution of inclusions in sector-zoned crystals it is possible to infer a rhombododecahedral shape for the garnet. This is confirmed by the μCT analysis, where the well-developed euhedral shape of the crystals can be best appreciated (Fig. 4.44, Fig 4.45 and Fig 4.46).

Ilmenite is observed with 2D rectangular sections, and very often develops quartz and chlorite strain shadows (Fig. 4.29 and 4.30) where chlorite is clearly stable and in microstructural equilibrium. μCT reveals a tabular coin-shaped habit for ilmenite, with sometimes a pseudo-hexagonal outline (Fig. 4.47 and Fig 4.48). Many ilmenite crystals seem to be iso-oriented parallel to the schistosity (Fig 4.49).

5.2 Previous studies

The available literature on similar microstructures is very limited and not much work has been done on the subject of this thesis. Only Lister et al. (1985), Miyake (1992), Little et al. (2002), Kim and Cho (2008) and Camilleri (2009) have reported similar microstructures.

Lister et al. (1985) highlight the presence of inner graphite-rich "dirty" zones and outer clear zones in biotite porphyroblasts and also the presence of chlorite in both zones, suggesting a possible stiffening of the porphyroblast caused by the presence of graphite inclusions sealing the cleavage planes of the phyllosilicates (G. Lister, personal communication). Their interpretation of the microstructure is that biotite rotated due to non-coaxial (simple) shear where all biotite crystals were obliquely oriented in the matrix and depending on the forward- or back-inclined position of the crystals with respect to the sense of shear. This resulted in fish-like shapes if biotite clevage was perpendicular with respect to the foliation or forward-inclined with respect to stress, and in tabular shapes if it was back-inclined with respect to the stresss. In both cases the biotites would show rotated

inclusion trails (Fig. 5.1). Lister et al (1985) also proposed a crack-seal mechanism for step-wise dilation of biotite, caused by fluctuating pore fluid pressure that resulted in alternating cracks and deposition of biotite by fluids coming from prograde and retrograde reactions. In their work, chlorite and biotite intergrowths were detected in both dirty and clear sectors by TEM. This feature is found to be common in both low-grade and higher grade metapelites (Lee et al., 2002).
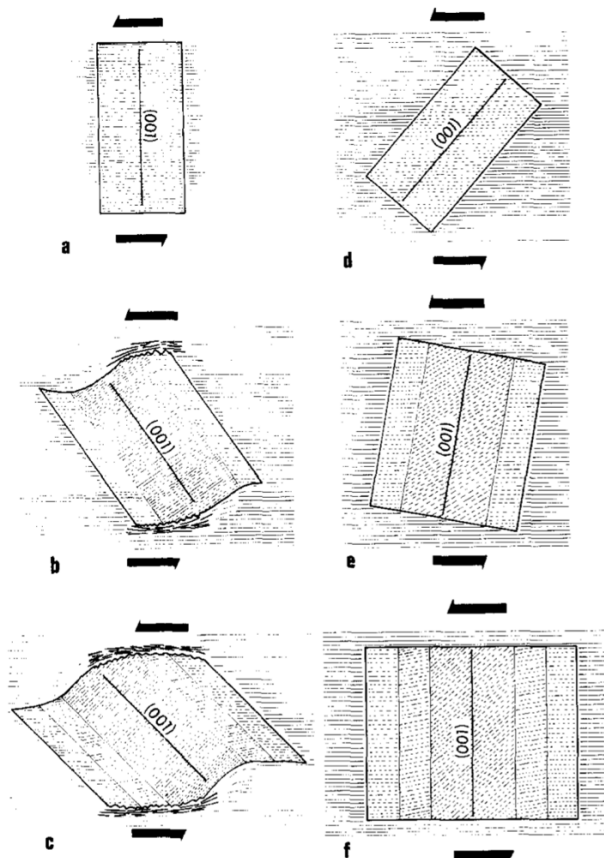
Fig. 5.1: biotite porphyroblasts rotation under simple shear deformation after Lister et al. (1985). Sequence a-c shows the development of fish-like shapes and sequence d-f shows the development of tabular shapes. Rotation causes obliquity of parts of internal foliation with respect to the external one.

Miyake (1993) went deeper into the rotation of biotite porphyroblasts, stating that in the investigated samples there were no sign of intracrystalline slip. He also argued, in the same fashion as Lister, that inclusions may result in the stiffening of the crystals. Strain shadows caused by rotation of biotite are recorded as clear zones on both ends of crystals. The new biotite grown in the pressure shadows during deformation is thought to be the result of mass-transfer due to pressure-solution. Miyake demonstrated the possible microstructures (Fig. 5.2) that can result from both coaxial (pure) and non-coaxial shear, implying that rotation can take place under pure shear.
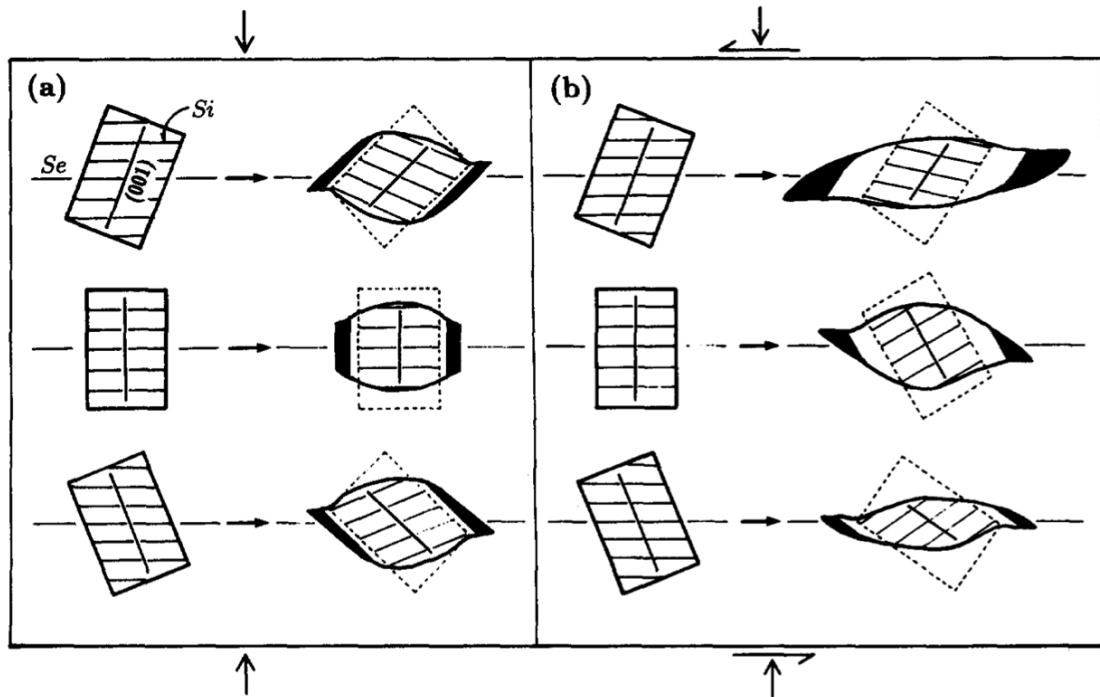
Fig. 5.2: biotite porphyroblasts rotation under pure shear deformation (a) and simple shear deformation (b). "Se" stands for surrounding foliation and "Si" stands for inclusion trails. Figure after Miyake (1993).

The microstructures described and discussed by Little et al. (2002) are nearly the same as those studied in this work (Fig. 5.3). They refer to them as microboudinaged biotites and show that the biotite affected by extensions are the porphyroblasts with the cleavage at high angle with respect to the foliation, with the original fragments of biotite marked by a continuous graphite inclusion trail. Despite a general oblate strain in their samples, some rocks are still preserving some sign of a maximum incremental stretch. This means that there are some evidences of prolate strain.
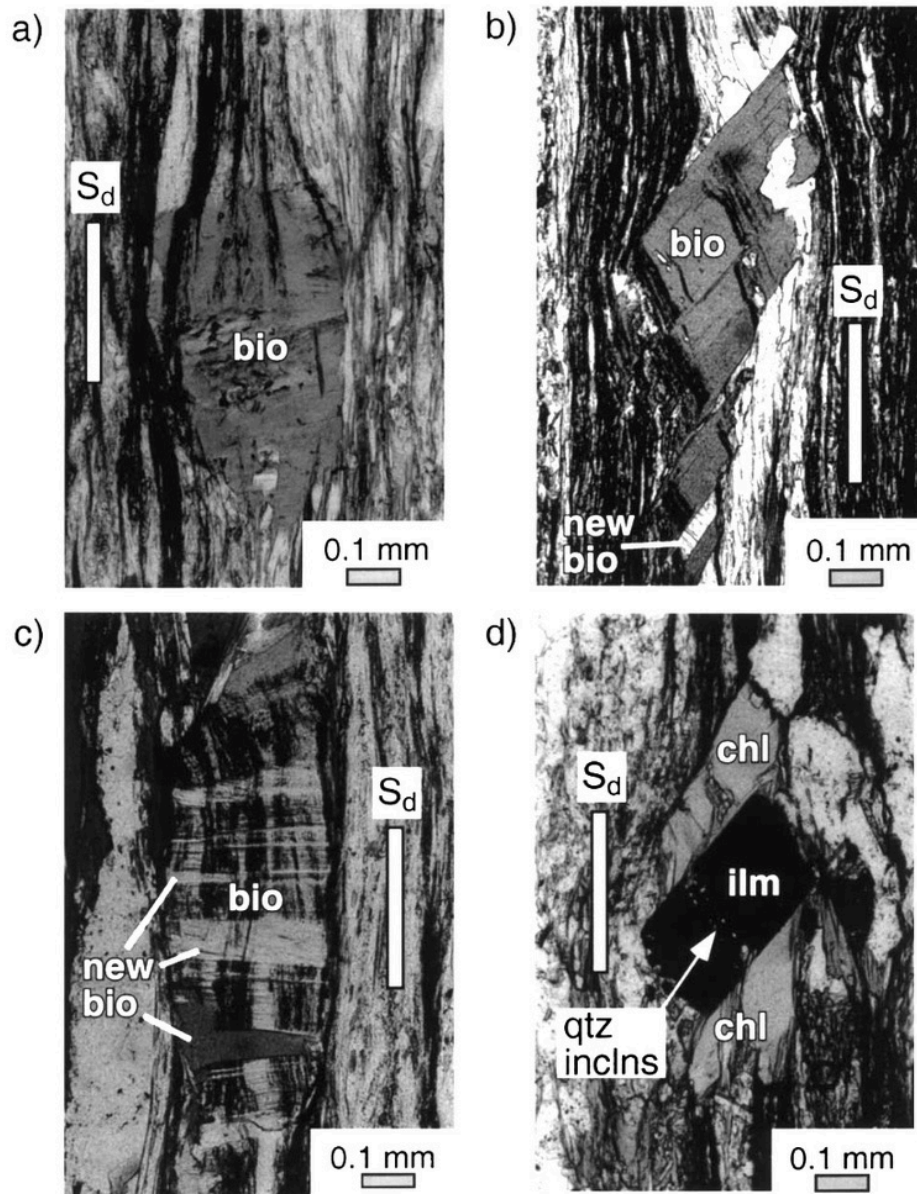
Fig. 5.3: biotite microstructures from Little et al. (2002). a: differential thickness of graphitic markers; b: bookshelf tilting and rotation of biotite; c: microboudinage of biotite; d: ilmenite strain shadow. Sd indicated the dominant foliation.

The work by Camilleri (2009), argued that biotites with cleavage at a high angle with respect to the foliation is a very unusual occurrence in phyllosilicates. She proved that biotite porphyroblasts in undeformed zones does not show any preferred growth orientation and high angle cleavages with respect to the foliation are common. Instead, sheared zones are showing oblique and parallel cleavages in respect to the foliation. She also showed how inclusions in biotite may result in sector zoning of the crystals.

5.3 Origin of type I biotites

What is seen in the rock is a strong extension that caused the microboudinage of the crystals with subsequent precipitation crystallization of new biotite and quartz inside the necks; the original pre-boudinage crystals can be identified thanks to their continuous graphite inclusions, whereas the biotite and quartz newly grown within necks are inclusion free. In addition, chlorite and biotite intergrowths identify the original sectors from the newly grown one.

Extension was a consequence of pure shear deformation, since type II biotites are showing both dextral and sinistral shear sense in equal measure. This agrees with what Miyake (1993) described (Fig. 5.2) since the internal foliation inclusion patterns coincide with the one observed in this work.

As high angle cleavages with respect to the foliation in phyllosilicates (and so in biotite) are rare in strained domains, it is possible to argue that in the studied rocks, where high-angle cleavages are frequent, biotite crystals nucleated in a static setting and were subsequently contemporaneously deformed and rotated. In static environments, biotite crystals grow randomly oriented in respect to the foliation (Camilleri, 2009).

Even though oblique fabrics are very rare and localized to the deformed foliation inside type II biotites, it is possible to say that a a maximum of 20-30° of rotation was attained.

A possible interpretation of the observed microstructures is that biotite with (001) at very high angle (type I) were, and are still now, the largest crystals and so they were very difficult to rotate with the very little rotation imposed to the whole rock mass.

Instead, fanned (type II) biotite are smaller and probably started their rotation with lower starting angles than type I biotites, meaning that were prone to rotate and that even with little imposed rotation, they have been able to achieve fanned shape (rotation after microboudinage). Another possible interpretation is the rotation of newly growth biotite during microboudinage. In this case (Fig. 5.4), the original starting biotite is inclined, in the same way as the previous model, but when it gets microboudinaged, new biotite precipitates and grows with (001) at high angles in respect to the foliation (contemporaneous rotation and microboudinage)
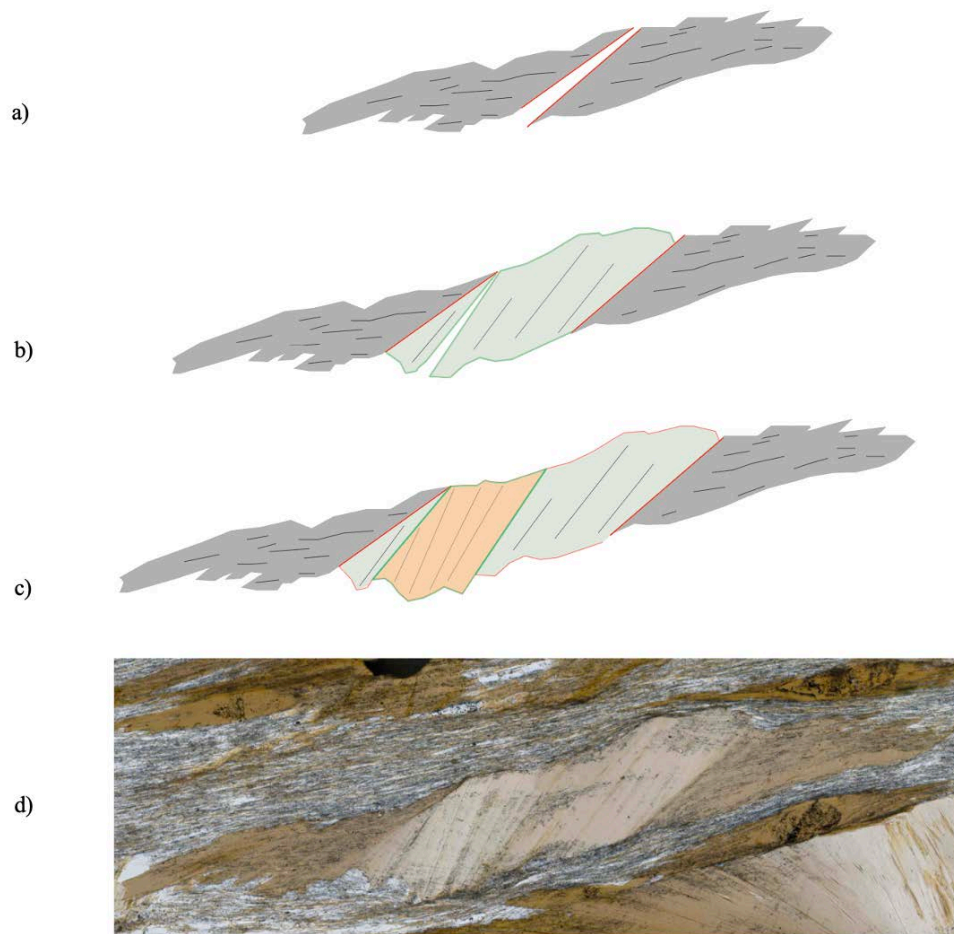
Fig. 5.4: development of type II biotites. a) original initial biotite; b) first increment with (001) at a high angle in respect to the foliation; c) second increment with (001) nearly perpendicular to the foliation; d) thin section view of the porphyroblast (2 mm long).

Elongated (type III) biotites didn't even experience rotation as they were probably originally grown in the same position in which are found now. It is also possible that type III biotites were very gently inclined at a small angle from the foliation, but it is not possible to know if the elongation is given by a syn-kinematic growth parallel to the microboudinage direction or if they were actually deformed due to extension.

The formation mechanism can be attributed to a combined pure shear deformation that resulted in extension and a small degree of rotation of the porphyroblasts with an initial random orientation of the crystals.

Biotite is the principal mineral that precipitates inside boudin necks and the X_{Mg} values show that only one generation of biotite is present from a chemical viewpoint. Quartz is found in boudin necks together with biotite, particularly in the highly strained (higher than 100%) biotites. This may indicate

that deformation was intense enough so that biotite was not able to keep up and quartz had to fill in the new space.

To summarize, the event that led to the formation of type I, II and III biotite porphyroblasts:

1) Random growth of biotite porphyroblasts in a static environment with inclusion of graphite from the matrix.

2) Pure shear deformation and faint rotation of the biotites:
   Type I: intense microboudinage and precipitation of biotite and quartz in type I necks with (very little rotation.

   Type II: combined rotation and microboudinage with biotite precipitation for type II biotites but with different rotation timing

   Type III: little to no rotation and only deformation/crystallization for type III biotites.

5.3.1 Metamorphism/deformation relations

From the relations between mineral growth and deformation, we can infer the relative timing of the events. Minerals can be pre-, inter-, syn- and post-tectonic (or kinematic) (Passchier & Trouw, 2005) based on the relations between porphyroblasts and the matrix around them. Pre-kinematic porphyroblasts are characterized by the presence of strain shadow and random distribution of inclusions; inter-tectonic porphyroblasts show internal foliation at high angle from the matrix and strain shadows; syn-kinematic porphyroblasts are usually showing continuous inclusion trails that are often curved and strain shadow; finally, post-kinematic porphyroblasts are showing no deflection of the matrix and no pressure shadow while inclusion trails are continuous with the foliation.

Only one deformation phase has been recorded in the studied rocks, and it is related to the microboudinage development (D_1). The mineral assemblage commonly developed in the schists (Qz-Pl-Bt-Grt-Ms-Chl-Ilm-Gr±Ep±St), and the chemical composition of phases (S. Bedon, personal communication) indicate that the rocks nicely equilibrated during the Alpine metamorphism (M_1) under fairly homogeneous P-T conditions, without recording evidence of previous metamorphic

events. From the petrographic observations, it is possible to determine if the porphyroblasts are pre-, intra, syn- or post-kinematic in relation to the D_1 deformation phase.

Biotite is clearly pre-kinematic and syn-kinematic. Pre-kinematic biotite is the one that forms the original sectors of the coarse type I porphyroblasts and it is possible to state this because of the graphite inclusions trails that are continuous with the external foliation; this is also seen from the small biotite pressure shadow. Syn-kinematic biotite is instead the one that precipitates inside the necks during deformation.

Garnet can be defined as pre-to-syn kinematic. Continuous curved inclusion trails are clearly defining a syn-kinematic porphyroblasts, however sector zoning may signify both pre-kinematic and syn-kinematic porphyroblasts. In places, the thin garnet rims overgrowing the foliation at strain caps attest for a modest post-kinematic garnet growth.

Ilmenite is clearly pre-kinematic. Nearly all the porphyroblasts are aligned and the presence of strain shadow indicates a rotation of the crystals. The pseudo-hexagonal subhedral shape is also suggesting a pre-kinematic growth.

Other minerals such as quartz, plagioclase, epidote, muscovite and chlorite are in part probably preceding the formation of the porphyroblasts because we observe quartz and epidote inclusions inside garnet and bent phyllosilicates in strain caps. Nonetheless, since phyllosilicates crystals are well oriented in the matrix and do not show curves shapes, it is possible that the whole matrix was syn-kinematically recrystallized. Chlorite and quartz are also syn-kinematic as the latter can be found in the neck of type I porphyroblasts and both are found inside ilmenite strain shadows.
The rare staurolite crystal show a light deflection of the surrounding foliation and so are syn-kinematic.

The timing relation is described by Fig. 5.5:

	Pre-kinematic M_1	Syn-kinematic M_1/D_1	Post-kinematic M_1
Biotite	———————————————		
Garnet	————————————————————————		
Ilmenite	————————		
Quartz	———————————————		
Muscovite	———————————————		
Plagioclase	———————————————		
Chlorite	———————————————		
Staurolite		————————	
Graphite	————————		
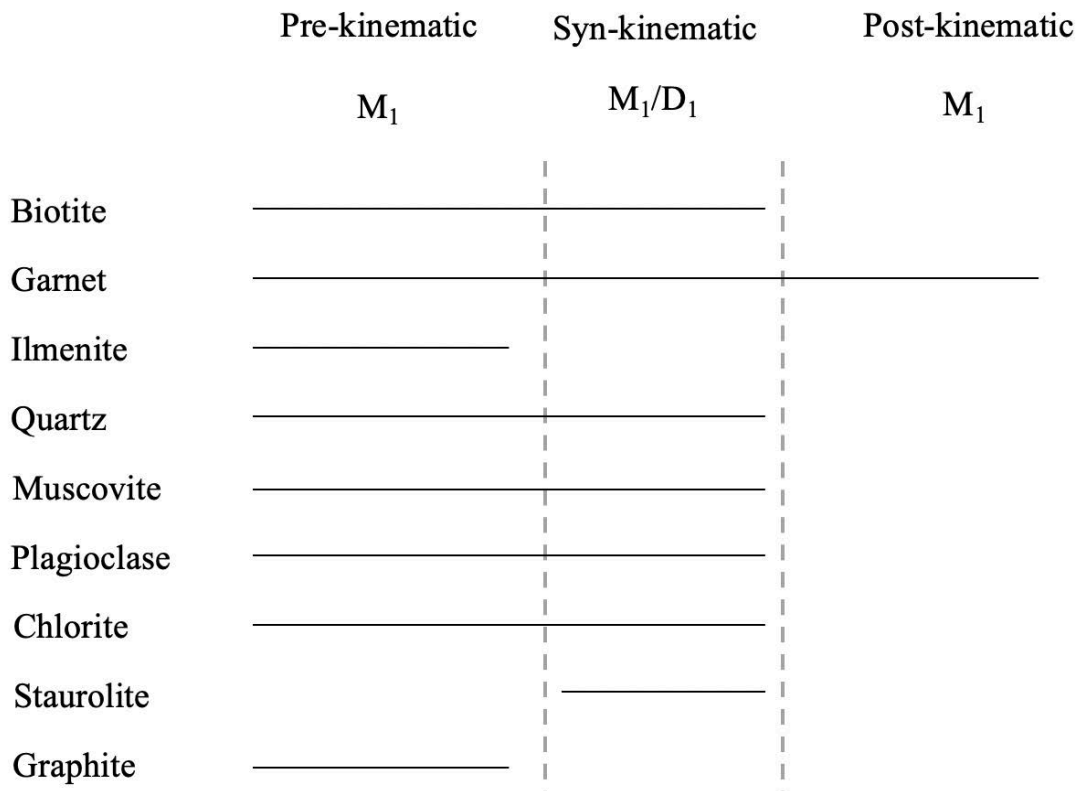
Fig. 5.5: metamorphism and deformation relations. M_1 represents Alpine metamorphism that is active before, during and after the deformation phase D_1.

The analyzed microstructures provide insights on the behaviour of biotite porphyroblasts, but they are also part of a bigger picture of the tectonics of the Tauern Window.

As stated in Chapter 2, the whole TW was subjected to a NNE directed indentation (Rosenberg et al., 2004) that caused an orogen-perpendicular shortening and an orogen-parallel extension (Rosenberg et al., 2004; Schmid et al., 2013). The TW is roughly EW oriented (Fig 2.1, 2.2 and 2.4) and the structural measurements collected on the outcrop show an E-W lineation with an average trend of 265N and a plunge of 20°.

Since microboudinaged biotites are deforming, and so extending, parallel to the foliation, then it is possible to say that type I biotite formed in response to the large scale orogen-parallel extension.

6 Conclusions

The results of this work can be divided in two categories. The first concerns the definition of the deformation mechanism that formed the analyzed microstructures while the second concerns the application of μCT data for rock microstructural analysis.

The deformation mechanism has been thought to be a combination of microboudinage and rotation of the porphyroblasts. Type I biotite forms due to microboudinage and precipitation of new biotite and quartz in the necks but with very little rotation of the porphyroblasts. Type II biotite is instead more prone to rotation, but the timing of rotation is not clear and may be antecedent or contemporaneous to the microboudinage. Type III biotites formation is also debated as they may have been elongated due to new growth or due to deformation.

The deformation mechanisms for type I and type II biotites are consistent with what the rotation and crack-seal mechanism described by Lister et al. (1985), the pure shear rotation microstructures describe by Miyake (1993) and the microboudinage microstructures described by Little et al. (2002).

μCT is not a routine analytical technique but our results are showing how important the 3D analysis is for rock microstructure definition and interpretation. 3D data should always be integrated to 2D observations as porphyroblasts develop in three dimensions; in this way, it is possible the get a complete view of the porphyroblasts shape and orientation. The 3D renders aid the visualization, help the definition of the microstructure as a whole and confirms many 2D observation that otherwise would have not been evident.

3D image analysis also permits to collect quantitative data of the orientation, elongation and shape of the porphyroblasts. In this work, we performed a fabric analysis on the overall shape of biotite and ilmenite porphyroblasts by plotting the concentrations of biotite long axes and ilmenite long and intermediate axes in order to understand the relation between the microfabric and the porphyroblasts

In the future, more measurements of rotated inclusion trails could be performed in order to solve the relative timing of the rotation during the development of type II biotites. It could also be interesting to actually determine a minimum length at which biotite rotation starts to rotate. This would help in an even better definition of the deformation mechanism that acted on the Furtschaglschiefer unit.

References

Baggio, P., De Vecchi, G, Mezzacasa, G (1975): Carta geologica della media ed alta Valle di Vizze e regioni vicine (Alto Adige), 1:25.000. *Consiglio Nazionale delle Ricerche, Padova*.

Camilleri, P. A. (2009). *Growth, behavior, and textural sector zoning of biotite porphyroblasts during regional metamorphism and the implications for interpretation of inclusion trails: Insights from the Pequop Mountains and Wood Hills, Nevada, USA*.

Cesare, B., Nestola, F., Johnson, T., Mugnaioli, E., Della Ventura, G., Peruzzo, L., Bartoli, O., Viti, C., & Erickson, T. (2019). Garnet, the archetypal cubic mineral, grows tetragonal. *Scientific Reports*, *9*(1), 14672. https://doi.org/10.1038/s41598-019-51214-9

Cesare, B., Rubatto, D., Hermann, J., & Barzi, L. (2002). Evidence for Late Carboniferous subduction-type magmatism in mafic-ultramafic cumulates of the SW Tauern window (Eastern Alps). *Contributions to Mineralogy and Petrology*, *142*(4), 449–464. https://doi.org/10.1007/s004100100302

Christensen, J. N., Selverstone, J., Rosenfeld, J. L., & DePaolo, D. J. (1994). Correlation by Rb-Sr geochronology of garnet growth histories from different structural levels within the Tauern Window, Eastern Alps. *Contributions to Mineralogy and Petrology*, *118*(1), 1–12. https://doi.org/10.1007/BF00310607

Cnudde, V., & Boone, M. N. (2013). High-resolution X-ray computed tomography in geosciences: A review of the current technology and applications. *Earth-Science Reviews*, *123*, 1–17. https://doi.org/10.1016/j.earscirev.2013.04.003

da Mommio, A. (2018). Evoluzione metamorfica delle unità paraderivate nella Finestra dei Tauri Occidentale

Dal Piaz, G. V., Bistacchi, A., & Massironi, M. (2003). Geological outline of the Alps. *Episodes Journal of International Geoscience*, *26*(3), 175-180.

De Vecchi, G., e Baggio, P. (1982). The Pennine zone of the Vizze region in the western Tauern window (Italian eastern Alps). Bollettino della Societa Geologica Italiana, 101(1), 89-116.

Exner, V. C. (1964). *Erläuterungen zur Geologischen Karte der Sonnblickgruppe*.

Exner C (1971) Geologie der peripheren Hafnergruppe (Hohe Tauern). Jahrb Geol Bundesanst 114: 1–119

Exner, V. C. (1979). *Geologie des Salzachtales zwischen Taxenbach und Lend*.

Franz, G., Kutzschbach, M., Berryman, E. J., Meixner, A., Loges, A., & Schultze, D. (2021). Geochemistry and paleogeographic implications of Permo-Triassic metasedimentary cover from the Tauern Window (Eastern Alps). *European Journal of Mineralogy*, *33*(4), 401–423. https://doi.org/10.5194/ejm-33-401-2021

Friedrichsen, H., & Morteani, G. (1979). Oxygen and hydrogen isotope studies on minerals from alpine fissures and their gneissic host rocks, Western Tauern Window (Austria). *Contributions to Mineralogy and Petrology*, *70*(2), 149–152. https://doi.org/10.1007/BF00374443

Frisch., W., e Raab, D. (1987). Early Paleozoic back arc and island arc settings in greenstone sequences of the Central Tauern Window (Eastern Alps). *Jahrbuch der Geologischen Bundesanstalt 129*, 545-566.

Frisch, W., Dunkl, I., & Kuhlemann, J. (2000). Post-collisional orogen-parallel large-scale extension in the Eastern Alps. *Tectonophysics*, *327*(3–4), 239–265. https://doi.org/10.1016/S0040-1951(00)00204-3

Hobbs, B. E., Ord, A., Spalla, M. I., Gosso, G., & Zucali, M. (2010). The interaction of deformation and metamorphic reactions. *Geological Society, London, Special Publications*, *332*(1), 189–223. https://doi.org/10.1144/SP332.12

Höck, V. (1983). Mesozoic ophiolites and non-ophiolitic metabasites in the central part of the Tauern Window (eastern Alps, Austria)

Hoernes, S. T., e Friedrichsen, H. (1974). Oxygen isotope studies on metamorphic rocks of the western Hohe Tauern area (Austria). *Schweizerische Mineralogische und Petrographische Mitteilungen, 54*, 769-788.

Ketcham, R. A. (2005). Three-dimensional grain fabric measurements using high-resolution X-ray computed tomography. *Journal of Structural Geology*, *27*(7), 1217–1228. https://doi.org/10.1016/j.jsg.2005.02.006

Kim, Y., & Cho, M. (2008). Two-stage growth of porphyroblastic biotite and garnet in the Barrovian metapelites of the Imjingang belt, central Korea. *Journal of Metamorphic Geology*, *26*(3), 385–399. https://doi.org/10.1111/j.1525-1314.2008.00767.x

Kurz, W., Neubauer, F., Genser, J., & Dachs, E. (1998). Alpine geodynamic evolution of passive and active continental margin sequences in the Tauern Window (eastern Alps, Austria, Italy): A review. *Geologische Rundschau*, *87*(2), 225–242. https://doi.org/10.1007/s005310050204

Lammerer, B., Gebrande, H., Lüschen, E., & Veselá, P. (2008). A crustal-scale cross-section through the Tauern Window (eastern Alps) from geophysical and geological data. *Geological Society, London, Special Publications*, *298*(1), 219–229. https://doi.org/10.1144/SP298.11

Lardeaux, J.-M. (2023). Metamorphism and linked deformation in understanding tectonic processes at varied scales. *Comptes Rendus. Géoscience*, *356*(S2), 1–25. https://doi.org/10.5802/crgeos.204

Lee, Y. B., Lee, J. H., & Oh, C. W. (2002). Intergrowth and Interlayering of Muscovite, Chlorite, and Biotite in a Garnet Zone Metamorphic Rock of the Ogcheon Belt, South Korea. *Journal of the Mineralogical Society of Korea*, *15*(2), 122-131.

Lister, G. S., Boland, J. N., & Zwart, H. J. (1986). Step-wise growth of biotite porphyroblasts in pelitic schists of the western Lys-Caillaouas massif (Pyrenees). *Journal of Structural Geology*, *8*(5), 543–562. https://doi.org/10.1016/0191-8141(86)90004-0

Little, T. A., Holcombe, R. J., & Ilg, B. R. (2002). Kinematics of oblique collision and ramping inferred from microstructures and strain in middle crustal rocks, central Southern Alps, New Zealandq. *Journal of Structural Geology*.

Miller, Ch., Satir, M., e Frank, W. (1980). High-pressure metamorphism in the Tauern Window. Mitteilungen der Österreichischen Geologischen Gesellschaft, 71(72), 89-97.

Misch, P. (1969). Paracrystalline microboudinage of zoned grains and other criteria for synkinematic growth of metamorphic minerals. *American Journal of Science*, *267*(1), 43-63.

Miyake, A. (1993). Rotation of biotite porphyroblasts in pelitic schist from the Nukata area, central Japan. *Journal of Structural Geology*, *15*(11), 1303–1313. https://doi.org/10.1016/0191-8141(93)90104-I

Passchier, C. W., & Trouw, R. A. J. (2005). *Microtectonics* (02 ed.). Springer.

Ratschbacher, L., Frisch, W., Neubauer, F., Schmid, S. M., & Neugebauer, J. (1989). Extension in compressional orogenic belts: The eastern Alps. *Geology*, *17*(5), 404. https://doi.org/10.1130/0091-7613(1989)017<0404:EICOBT>2.3.CO;2

Rice, A. H. N., Habler, G., Carrupt, E., Cotza, G., Wiesmayr, G., Schuster, R., ... & Koller, F. (2006). Textural sector-zoning in garnet: Theoretical patterns and natural examples from Alpine metamorphic rocks. *Australian Journal of Earth Sciences*, *6*, 70-89.

Romero-Zaliz, R., & Reinoso-Gordo, J. F. (2018). An Updated Review on Watershed Algorithms. In C. Cruz Corona (Ed.), *Soft Computing for Sustainability Science* (Vol. 358, pp. 235–258). Springer International Publishing. https://doi.org/10.1007/978-3-319-62359-7_12

Rosenberg, C. L., Brun, J.-P., & Gapais, D. (2004). Indentation model of the Eastern Alps and the origin of the Tauern Window. *Geology*, *32*(11), 997. https://doi.org/10.1130/G20793.1

Rutter, E. H., & Brodie, K. H. (1995). Mechanistic interactions between deformation and metamorphism. *Geological Journal*, *30*(3–4), 227–240. https://doi.org/10.1002/gj.3350300304

Sander, R. (1912). über einige Gesteinsgruppen des Tauernwestendes. *Verlag der kk geologischen Reichsanstalt.*

Sayab, M., Aerden, D., Kuva, J., & Hassan, W. U. (2021). Tectonic evolution of the Karakoram metamorphic complex (NW Himalayas) reflected in the 3D structures of spiral garnets: Insights from X-ray computed micro-tomography. *Geoscience Frontiers*, *12*(3), 101113. https://doi.org/10.1016/j.gsf.2020.11.010

Sayab, M., Suuronen, J.-P., Hölttä, P., Aerden, D., Lahtinen, R., & Kallonen, A. P. (2015). High-resolution X-ray computed microtomography: A holistic approach to metamorphic fabric analyses. *Geology*, *43*(1), 55–58. https://doi.org/10.1130/G36250.1

Schmid, S. M., Fügenschuh, B., Kissling, E., & Schuster, R. (2004). Tectonic map and overall architecture of the Alpine orogen. *Eclogae Geologicae Helvetiae*, *97*(1), 93–117. https://doi.org/10.1007/s00015-004-1113-x

Schmid, S. M., Scharf, A., Handy, M. R., & Rosenberg, C. L. (2013). The Tauern Window (Eastern Alps, Austria): A new tectonic map, with cross-sections and a tectonometamorphic synthesis. *Swiss Journal of Geosciences*, *106*(1), 1–32. https://doi.org/10.1007/s00015-013-0123-y

Selverstone, J. (1985). Petrologic constraints on imbrication, metamorphism, and uplift in the SW Tauern Window, eastern Alps. *Tectonics*, *4*(7), 687–704. https://doi.org/10.1029/TC004i007p00687

Selverstone, J. (1988). Evidence for east-west crustal extension in the Eastern Alps: Implications for the unroofing history of the Tauern window. *Tectonics*, *7*(1), 87–105. https://doi.org/10.1029/TC007i001p00087

Selverstone, J., Spear, F. S., Franz, G., & Morteani, G. (1984). High-Pressure Metamorphism in the SW Tauern Window, Austria: P-T Paths from Hornblende-Kyanite-Staurolite Schists. *Journal of Petrology*, *25*(2), 501–531. https://doi.org/10.1093/petrology/25.2.501

Selverstone, J., & Spear, F. S. (1985). Metamorphic P–T paths from pelitic schists and greenstones from the south-west Tauern Window

TRANSALP Working Group, Gebrande, H., Lüschen, E., Bopp, M., Bleibinhaus, F., Lammerer, B., Oncken, O., Stiller, M., Kummerow, J., Kind, R., Millahn, K., Grassl, H., Neubauer, F., Bertelli, L., Borrini, D., Fantoni, R., Pessina, C., Sella, M., Castellarin, A., … Bernabini, M. (2002). First deep seismic reflection images of the Eastern Alps reveal giant crustal wedges and transcrustal ramps: FIRST DEEP SEISMIC REFLECTION IMAGES OF THE EASTERN ALPS REVEAL GIANT CRUSTAL WEDGES AND TRANSCRUSTAL RAMPS. *Geophysical Research Letters*, *29*(10), 92-1-92–94. https://doi.org/10.1029/2002GL014911

Veselá, P., & Lammerer, B. (2008). The Pfitsch-Mörchner Basin, an example of the post-Variscan sedimentary evolution in the Tauern Window (Eastern Alps). *Swiss Journal of Geosciences*, *101*(S1), 73–88. https://doi.org/10.1007/s00015-008-1293-x

Whitney, D. L., & Evans, B. W. (2010). Abbreviations for names of rock-forming minerals. *American Mineralogist*, *95*(1), 185–187. https://doi.org/10.2138/am.2010.3371

Zwart, H. J. (1962). On the determination of polymetamorphic mineral associations, and its application to the Bosost Area (Central Pyrenees). *Geologische Rundschau*, *52*(1), 38–65. https://doi.org/10.1007/BF01840064